energies

MDPI

Article

Power and Fatigue–Load Assessment of Static Wake Steering in a Floating Wind Farm with 15 MW Turbines

Majid Ebrahimi, Federico Bellini, Alessandro Fontanella *, Sara Muggiasca and Marco Belloli

Department of Mechanical Engineering, Politecnico di Milano, Via La Masa 1, 20156 Milano, Italy
* Correspondence: alessandro.fontanella@polimi.it

Abstract

Static wake steering can increase wind-farm power production, but its application to floating offshore wind farms requires assessment of the coupled wake, platform, structural, and station-keeping response. This study evaluates whether power-maximizing static yaw setpoints identified using the steady, control-oriented FLORIS model retain their benefit when transferred without re-optimization to a coupled FAST.Farm floating wind-farm model. The reference farm comprises four IEA Wind 15 MW turbines mounted on VolturnUS-S semi-submersible platforms. Greedy and static wake-steering operations are compared at three below-rated wind speeds, three sea states, and five matched turbulent-inflow realizations, resulting in 90 farm-level FAST.Farm simulations. Wake behavior is characterized through wake-center deflection, meandering, and velocity-deficit profiles, while turbine and mooring fatigue responses are evaluated using paired damage-equivalent-load statistics. Static wake steering increases mean farm power under all nine investigated wind–wave conditions. The gains are approximately 5.1–5.2% at 7 $\mathrm{m\,s^{-1}}$, 5.0–5.1% at 8 $\mathrm{m\,s^{-1}}$, and 4.0–4.2% at 9 $\mathrm{m\,s^{-1}}$, with all paired 95% confidence intervals remaining above zero. The gain results from a power redistribution in which the intentionally yawed upstream turbine incurs a local loss that is exceeded by the combined recovery of the downstream turbines. The fatigue response is strongly component- and turbine-dependent. The paired farm-mean blade-root DEL decreases by 0.82–2.24%, whereas the tower-base DEL increases by 0.76–2.78%, and the FairTen1 response generally increases by 0.88–2.92%. The farm-mean yaw-bearing response is mixed, ranging from a 1.15% reduction to a 4.32% increase. Turbine-level analysis reveals larger localized penalties, reaching approximately 10.4% for the yaw-bearing DEL and 12.8% for FairTen1. Spectral analysis associates the yaw-bearing response with yaw-induced aerodynamic and structural excitation, while the tower-base response is strongly influenced by low-frequency wave–platform dynamics. A complementary FLORIS sensitivity analysis demonstrates that the optimized aerodynamic benefit depends strongly on wind direction, spacing, wind speed, and turbulence intensity. For a Tampen-derived 11-turbine layout, resource weighting over the modeled 4–13 $\mathrm{m\,s^{-1}}$ interval produces an annual energy-contribution increase of 3.653 GWh $\mathrm{year^{-1}}$, or 0.921%. These results provide numerical evidence that static wake steering can retain a positive power benefit in a coupled floating wind-farm environment, but controller assessment must include turbine- and component-specific dynamic loads rather than farm power alone.

Keywords: floating offshore wind farm; wake steering; FAST.Farm; FLORIS; ROSCO; ZeroMQ; dynamic wake meandering

Academic Editor: Lars Johanning

Received: 1 July 2026
Revised: 8 August 2026
Accepted: 17 August 2026
Published: 21 August 2026

1. Introduction

Wake interactions are a defining feature of wind-farm operation. Upstream turbines extract momentum from wind and generate wakes characterized by reduced wind speed and increased turbulence. These wakes reduce the power production of downstream turbines and can increase structural loading. Wake losses can reduce farm-level energy capture by approximately 10–20% in large arrays [1,2] and accelerate fatigue damage in downstream turbines [3]. Consequently, greedy operation, in which each turbine aligns with the incoming wind and independently maximizes its own power production, is generally suboptimal at the wind-farm level.

Wind-farm control addresses the limitations of greedy operation by coordinating multiple turbines to increase energy production of a plant, reduce structural loading, and achieve a favorable trade-off between these competing objectives [4–6]. The two principal flow-control strategies are axial-induction control and yaw-based wake steering. Axial-induction control modifies the thrust and power extraction of upstream turbines to influence wake development and energy recovery. Although induction-control strategies have shown promising numerical and experimental trends, their robust field-scale benefits remain uncertain [7–10]. The present study therefore focuses on yaw-based wake steering as the more mature near-term strategy.

Yaw-based wake steering intentionally misaligns selected upstream turbines with the incoming wind direction to redirect their wakes away from downstream turbines. Although yaw misalignment typically reduces the power production of the yawed turbine, this local loss can be offset by increased production from downstream turbines experiencing reduced wake overlap [11,12]. The resulting wake response is more complex than a rigid lateral displacement. Yaw misalignment induces cross-flow velocities and counter-rotating vortical structures that deform the wake into an asymmetric curled, or kidney-bean-shaped, velocity-deficit distribution [11,13,14]. Interactions among these vortical structures, rotor-induced wake rotation, and vertical wind shear can also produce differences in wake deflection and wake evolution depending on the sign of the yaw-angle misalignment [12,14].

In addition to the mean deformation of the wake shape, the instantaneous trajectory of a steered wake is strongly influenced by turbulent inflow. Large-scale, low-frequency turbulent structures cause the wake to meander about its mean trajectory [15], while cross-stream velocity fluctuations and local variations in wind direction produce time-varying rotor-effective wind skew and corresponding variations in wake deflection [16,17]. Wake-steering assessment should therefore consider not only mean wake displacement, but also instantaneous wake meandering, wake-shape deformation, deficit recovery, and the resulting unsteady inflow experienced by downstream turbines.

Wake steering can also affect turbine loading. Intentional yaw misalignment introduces asymmetric aerodynamic loading on the yawed turbine, with effects on fatigue and extreme-load responses depending on the turbine component, operating condition, and inflow characteristics [18]. For downstream turbines, reduced wake overlap may decrease wake-turbulence-induced loading, whereas partial-wake exposure can increase cyclic rotor loading as the blades repeatedly pass between waked and unwaked regions [19]. FAST.Farm studies have shown that wake-steering-induced load changes depend on turbine position, load component, and yaw direction [20,21]. Therefore, power-maximizing yaw settings are not necessarily optimal when component-level fatigue loading is also considered.

Wake interactions are more complex in floating offshore wind farms than in bottom-fixed wind farms. Platform motions continuously modify the position and orientation of the rotor relative to the incoming flow, thereby changing the rotor-effective wind

https://doi.org/10.3390/en19163938

speed and direction. These motions alter wake position and recovery and produce turbine-to-turbine interactions that differ from those observed in bottom-fixed wind farms. Ramos et al. [22] showed that floater motion accelerates the breakdown of wake vertical structures and increases the unsteadiness of downstream turbine interactions with wakes. Similarly, Carmo et al. [23] demonstrated that mean platform pitch modifies vertical wake deflection and that wave-induced motions introduce dynamic responses absent from an equivalent fixed-bottom configuration. More recently, Liu et al. [24] used coupled SOWFA–OpenFAST simulations to investigate static yaw control for floating offshore wind turbines, considering rotor power, platform motion, wake characteristics, and fatigue loads. Zhang et al. [25] further showed that yaw angle and wave incident angle can jointly affect power production, platform motion, structural loads, and flow-field distribution in a semi-submersible floating wind-turbine array. In wake-steering applications, these aerodynamic effects combine with hydrodynamic excitation, low-frequency platform motions, turbine structural response, and station-keeping-system dynamics. Consequently, conclusions obtained for bottom-fixed wind farms cannot be transferred directly to floating wind farms without accounting for the coupled wake, structural, platform, and mooring response.

High-fidelity wind farm simulation approaches such as large-eddy simulation resolve detailed yawed-wake development and turbine-to-turbine interactions [13,22,26]. However, their computational cost limits their direct use for wind-farm-control design and systematic performance assessment. Control design requires repeated evaluation of numerous candidate yaw settings, whereas controller assessment requires simulations across multiple wind speeds, wind directions, turbulence conditions, sea states, wave directions, and turbulent-inflow realizations. Performing this complete design and evaluation matrix using high-fidelity coupled simulations would therefore be generally computationally impractical.

Steady control-oriented wake models and coupled dynamic wind-farm models provide complementary capabilities. Steady-state wake models can efficiently explore the multidimensional yaw-control space, defined by the yaw offsets assigned to each controllable turbine within prescribed bounds for a given wind speed and wind direction, and identify promising farm-level yaw setpoints [27]. However, they do not resolve wake meandering, time-varying deflection caused by turbulent rotor-effective wind skew and floating-platform motion, nor do they provide the structural and mooring-load time histories required for fatigue assessment. Conversely, coupled dynamic wind-farm models represent unsteady wake propagation together with turbine structural response, hydrodynamic loading, platform motion, and response of the station-keeping system, but remain computationally expensive for repeated optimization over large control spaces.

The present framework therefore uses FLORIS for efficient yaw-setpoint optimization and FAST.Farm for coupled dynamic assessment of wake behavior, power production, structural response, and mooring loads [17,28].

Recent studies have increasingly extended wake-steering analysis to floating wind-farm configurations. Rivera-Arreba et al. [29] compared FAST.Farm predictions with large-eddy simulations for the IEA Wind 15 MW turbine under yaw and tilt misalignment, considering wake-deficit evolution, mean wake deflection, and wake-meandering characteristics. Carmo et al. [23] examined the influence of platform pitch and wave-induced motion on floating-wake development, while Thedin et al. [20,21] investigated turbine-level fatigue–load responses and component-dependent power–load trade-offs under wake steering. Liu et al. [24] and Zhang et al. [30] considered coupled static-yaw operation in floating turbine and farm configurations, and Mohammadi et al. [31] recently combined power, load, and economic considerations for a larger floating array. These studies demonstrate the growing maturity of floating wind-farm wake-steering research;

however, assessments in which power-maximizing static yaw setpoints are transferred from a steady control-oriented model to a coupled dynamic floating wind-farm model remain limited, particularly when turbine-level power redistribution, structural fatigue, and mooring-line fatigue are evaluated simultaneously across multiple sea states.

The objective of the present study is to determine whether static wake-steering setpoints identified using a steady, control-oriented wake model to maximize wind-farm power retain their farm-level power benefit when evaluated in a coupled dynamic floating wind-farm environment.

This study follows a multi-fidelity assessment framework. First, a focused single-turbine FAST.Farm wake-characterization study is performed to examine the influence of the imposed yaw misalignment and selected wake-model parameter on the wake deflection, wake meandering, wake shape evolution, and downstream velocity-deficit recovery. This analysis is used to support the reference parameterization adopted in the subsequent farm-level simulations; it is not intended as a global sensitivity analysis of all environmental, numerical, and controller inputs. A four-turbine wind farm composed of IEA Wind 15 MW turbines mounted on VolturnUS-S semi-submersible platforms [32] is then considered. Static power-maximizing yaw setpoints are identified using FLORIS and transferred without re-optimization to FAST.Farm through ROSCO, where they are compared with greedy operation across multiple below-rated wind speeds, sea states, and turbulent-inflow realizations. The coupled simulations evaluate the retained farm-power benefit, turbine-level power redistribution, component-level fatigue loads, and mooring response.

The aerodynamic power analysis is subsequently extended in FLORIS to quantify how the predicted wake-steering benefit varies with turbine spacing, wind direction, wind speed, and ambient turbulence intensity. Finally, resource-weighted annual energy-contribution assessment is performed for an 11-turbine layout derived from the Hywind Tampen configuration [33]. The Tampen-derived coordinates are populated with IEA Wind 15 MW reference turbines, while the site wind climate is characterized using wind-speed and wind-direction data extracted from the NORA3 atmospheric hindcast at 150 m over the period of 2001–2020 [34,35].

The main contributions of this study are:

1. Assessment of whether static power-maximizing yaw setpoints obtained using a steady control-oriented wake model retain their farm-level benefit when transferred without re-optimization to a coupled dynamic floating wind-farm model, together with quantification of the resulting turbine-level power redistribution and component-specific fatigue–load changes in the blades, tower, yaw bearing, and mooring system;
2. Characterization of the single-turbine FAST.Farm wake response to imposed yaw misalignment and selected curled-wake parameter in terms of wake deflection, wake meandering, wake-shape evolution, and downstream velocity-deficit recovery;
3. Assessment of the aerodynamic sensitivity and practical energy significance of the predicted wake-steering benefit through a parametric analysis of turbine spacing, wind direction, wind speed, and ambient turbulence intensity, followed by a resource-weighted annual energy-contribution assessment for a larger Tampen-derived wind-farm layout.

2. Methodology

2.1. Numerical Models and Control Architecture

2.1.1. Reference Turbine and Floating Platform

The system considered in this work is the IEA Wind 15 MW reference wind turbine [36] mounted on the VolturnUS-S semi-submersible platform [32]. The principal turbine properties are summarized in Table 1, while the main platform, mooring-system, and natural-frequency properties are reported in Table 2.

Table 1. IEA Wind 15 MW reference-turbine parameters.

Parameter	Value	Units
Power rating	15	MW
Cut-in wind speed	3	m/s
Rated wind speed	10.59	m/s
Cut-out wind speed	25	m/s
Design tip-speed ratio	9.0	-
Minimum rotor speed	5.0	rpm
Maximum rotor speed	7.56	rpm
Rotor diameter	240	m

Table 2. Reference natural frequencies of the IEA Wind 15 MW–VolturnUS-S system. Values are taken from the work of Allen et al. [32].

Mode	Natural Frequency
Platform surge and sway	0.007 Hz
Platform yaw	0.011 Hz
Platform roll and pitch	0.036 Hz
Platform heave	0.049 Hz
First tower side-to-side/fore–aft bending	0.483/0.496 Hz

2.1.2. OpenFAST Aero-Hydro-Servo-Elastic Model

At the turbine level, each floating wind turbine is simulated in OpenFAST v4.2.0 using a coupled aero-hydro-servo-elastic model [37]. The model combines structural dynamics, aerodynamic loading, hydrodynamic loading, mooring-line dynamics, and turbine control. Structural dynamics are represented in ElastoDyn, aerodynamics in AeroDyn v15, hydrodynamic and wave loads in HydroDyn and SeaState, mooring-line dynamics in MoorDyn v2.3.8, and turbine control in ServoDyn through the Reference Open-source Controller (ROSCO) v2.9.0 [38].

The ElastoDyn model uses a combination of rigid-body and flexible coordinates. Rigid-body motions are represented through nodal displacements, while the flexible response of the blades and tower is represented using prescribed mode shapes. In the present configuration, 20 active degrees of freedom are retained: six platform rigid-body motions, four tower bending modes, nine blade modes, and one generator-azimuth degree of freedom. The blade modes include the first and second flapwise modes and the first edgewise mode for each blade, while the tower modes include the first and second fore–aft and side–side bending modes. This set of degrees of freedom captures the main rotor, tower, and platform motions that contribute to blade-root, tower-base, yaw-bearing moments and mooring-load variations.

Aerodynamic loads are computed in AeroDyn v15 using the blade-element momentum formulation. Tip-loss, hub-loss, tangential-induction, and drag contributions are included in the induction solution. Unsteady airfoil effects are represented using the Beddoes–Leishman Minnema/Pierce dynamic-stall model, while dynamic BEM wake effects are not activated. Since the present study includes yawed operation, the skewed-wake correction and skew-momentum correction are enabled to improve the representation of yawed and skewed inflow conditions.

Hydrodynamic loading is computed in HydroDyn, with incident wave conditions generated by SeaState. In the present configuration, SeaState generates irregular waves using a JONSWAP spectrum, and a wave heading of 0°. No current, directional spreading, or second-order wave kinematics are modeled. HydroDyn uses potential-flow hydrodynamics based on WAMIT data for the floating platform. Wave-excitation loads are evaluated using a formulation based on a discrete Fourier transform, and radiation memory effects are represented through convolution. Platform viscous damping is modeled through a quadratic damping matrix; strip-theory Morison members and second-order hydrodynamic loads are not included in the model.

The OpenFAST integration time step is set to $\Delta t = 0.025\,\mathrm{s}$. This turbine-level model is used inside FAST.Farm for each turbine in the array so that the wind-farm simulations retain the dominant aero-elastic, hydrodynamic, platform-motion, and mooring-load effects needed for the subsequent power– and fatigue-load assessment.

2.1.3. ROSCO Controller and ZeroMQ Supervisory Interface

Turbine-level control is implemented using the reference open-source controller ROSCO v2.9.0 through the ServoDyn DISCON interface [38]. ROSCO provides the turbine-level control functionalities–generator torque, collective blade pitch, and nacelle heading regulation–required for the OpenFAST simulations. In the present study, each turbine runs an independent ROSCO instance.

Farm-level yaw commands are imposed through the ROSCO–ZeroMQ communication interface [39]. In this client–server architecture, the external supervisory controller exchanges measurements and setpoints with the individual turbine controllers as illustrated in Figure 1. The supervisory command used in the present study is a static yaw-offset reference applied to T1–T3 in the wake-steering cases, whereas the greedy baseline is obtained by setting all supervisory yaw offsets to zero. In both strategies, the ROSCO yaw controller remains active, and the nacelle heading is therefore not fixed at its initial direction. The controller acts on the filtered yaw error using identical settings in all simulations, with $Y_{\mathrm{ErrThresh}} = 2^{\circ}$ and $F_{\mathrm{YawErr}} = 0.028\ \mathrm{rad\,s^{-1}}$. The filter and deadband limit unnecessary yaw activity caused by high-frequency turbulent fluctuations, while the wake-steering cases differ from the greedy baseline only through the additional prescribed supervisory yaw offset.

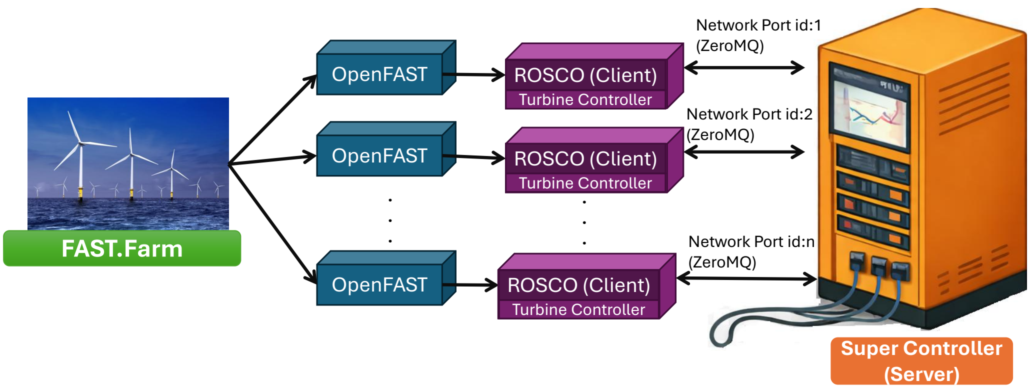

Figure 1. ROSCO–ZeroMQ supervisory-control architecture. Each turbine runs an independent ROSCO instance that exchanges turbine measurements and supervisory yaw-offset commands with the external farm-level controller through a client–server interface.

2.1.4. FAST.Farm Floating Wind-Farm Model

The floating wind farm is simulated using FAST.Farm v4.2.0, a mid-fidelity wind-farm simulation tool based on the dynamic wake meandering approach. In FAST.Farm, each turbine is represented by an individual OpenFAST model, while the farm-level solver describes the evolution of the wakes and their interaction with the ambient turbulent inflow. This approach allows the aero-hydro-servo-elastic response of each floating turbine to be modeled while accounting for wake advection, wake deflection, wake meandering, and turbine-to-turbine wake interactions at the farm scale.

The ambient inflow is supplied to FAST.Farm through multiple InflowWind instances. A low-resolution turbulent wind field spans the entire farm domain and provides the ambient flow used to model wake advection, deflection, meandering, and merging. Spatially and temporally synchronized high-resolution turbulent wind fields are defined around each turbine to provide the local inflow resolution required for aerodynamic and structural-response calculations in OpenFAST. This multi-resolution formulation reduces the computational cost of the wind-farm simulation while retaining the local spatial resolution required for aerodynamic and structural-load assessment.

Wake deficits are modeled using the FAST.Farm curl-wake formulation [17]. This formulation is used because the present study focuses on yaw-based wake steering in a floating wind farm. Under skewed inflow conditions, such as those caused by rotor misalignment due to rotor yaw or tilt, the wake is no longer axisymmetric. Instead, cross-flow velocities and curl-induced vorticity produce the characteristic curl or kidney-bean-shaped wake structure [17,40]. Mean platform translations shift the rotor position and hence the wake origin, whereas mean platform rotations modify the effective rotor orientation. In particular, mean platform pitch changes the effective rotor tilt and can produce additional vertical wake deflection [23,40]. The curl-wake formulation is therefore more appropriate for the present yawed floating-wake simulations than the polar formulation available in FAST.Farm, which assumes an axisymmetric wake structure.

2.1.5. FLORIS Wind-Farm Model and Static Yaw Optimization

FLORIS v3.6 is used in this work as a steady-state, control-oriented wind-farm model for computing static yaw-offset setpoints before their evaluation in FAST.Farm. This choice follows the multi-fidelity control framework of Bellini et al. [41], in which a FLORIS-based supervisory optimizer is coupled to a FAST.Farm floating wind-farm plant through a ZeroMQ communication interface.

The FLORIS wake model adopted in that framework is the Gaussian Curl Hybrid (GCH) model [42]. The model combines wake-deficit, wake-deflection, wake-added-turbulence, and wake-superposition formulations in a computationally efficient form suitable for repeated wind-farm-control optimization.

The GCH model structure and its FAST.Farm-oriented implementation were adopted following the work of Bellini et al. [41]. The yawed-turbine power exponent was fixed at $p_P = 1.2336$. A single common FLORIS configuration was then used throughout the present study. No wind-speed-, wind-direction-, turbulence-, spacing-, sea-state-, or layout-specific adjustment of the wake-model parameters was introduced between the reported analyses.

For each mean hub-height wind speed considered in the coupled four-turbine assessment, the static yaw-offset setpoints were computed using the serial-refine optimization algorithm proposed by Fleming et al. [43]. The optimization objective was to maximize the total steady-state farm power,

$$\gamma^*(U) = \arg\max_{\gamma} P_{\text{farm}}^{\text{FLORIS}}(U, \gamma), \tag{1}$$

subject to:

$$-20^\circ \leq \gamma_i \leq 20^\circ, \qquad i = 1, 2, 3, \qquad \gamma_4 = 0^\circ. \tag{2}$$

The design variables were the yaw offsets of the three upstream turbines, T1–T3. Turbine T4 was kept aligned with the incoming wind because no turbine was located downstream of it within the modeled four-turbine array.

The optimized setpoints were wind-speed-dependent but sea-state-independent because hydrodynamic excitation, irregular-wave loading, floating-platform motion, and structural response are not represented in FLORIS. Consequently, the same yaw-offset vector was applied to the mild, medium, and severe sea states at each wind speed.

The same fixed FLORIS configuration was also retained in the complementary four-turbine aerodynamic sensitivity analysis and in the Tampen-derived resource-weighted energy assessment. FLORIS is used in these analyses only to evaluate steady aerodynamic power and to select yaw setpoints; it is not used to infer structural loads, mooring loads, or unsteady wake-meandering statistics.

2.2. Single-Turbine FAST.Farm Wake-Model Characterization

The single-turbine wake-characterization simulations were conducted at $U = 8\ \mathrm{m\,s^{-1}}$ and TI $= 6\%$ as a controlled below-rated reference condition. In this operating region, turbine power remains sensitive to wake-induced changes in rotor-effective wind speed and yaw misalignment. The selected turbulence intensity represents a moderate offshore condition and is consistent with published offshore measurements and previous yaw-power sensitivity studies [44–46]. Holding wind speed and turbulence intensity fixed allows the effects of imposed yaw misalignment and the selected curl-wake parameter to be isolated. The analysis is therefore a focused wake-model characterization rather than a global sensitivity analysis of environmental, numerical, and controller parameters.

Two groups of cases were considered. First, imposed yaw-misalignment cases were used to characterize the mean wake-center displacement, wake meandering, and normalized velocity-deficit profiles. Second, selected curl-wake parameters, particularly $k_{v,\mathrm{curl}}$, were varied to examine their influence on wake spreading, recovery, and downstream wake shape.

2.2.1. Sensitivity Cases and Investigated Wake-Model Parameters

The single-turbine wake-characterization simulations were conducted at $U = 8\ \mathrm{m\,s^{-1}}$ and TI $= 6\%$ as a controlled below-rated reference condition. Holding the wind speed and turbulence intensity fixed allows the effects of the imposed nacelle–yaw misalignment and the selected curl-wake diffusion parameter to be examined independently. The analysis is therefore a focused wake-model characterization rather than a global sensitivity analysis of environmental, numerical, and controller parameters.

Two one-at-a-time sensitivity sweeps were performed. In the yaw-misalignment sweep, the imposed nacelle–yaw offset was varied, while the wake-model parameters were maintained at their reference values. In the wake-diffusion sweep, $k_{v,\mathrm{curl}}$ was varied, while the nacelle remained nominally aligned with the incoming wind. The reference settings and investigated values are summarized in Table 3. The reference-value column also defines the FAST.Farm wake-model configuration subsequently used in the coupled four-turbine simulations. In both sweeps, the floating-platform degrees of freedom remained active; therefore, the resolved wake response includes dynamically calculated platform translations and rotations, in addition to the imposed yaw-angle or wake-model-parameter variation.

https://doi.org/10.3390/en19163938

Table 3. Reference FAST.Farm settings and parameter values investigated in the single-turbine wake-characterization study. A dash indicates that the corresponding parameter was maintained at its reference value.

Setting	Reference Value	Investigated Values
Nacelle–yaw offset γ	$0°$	$[-20°, 20°]$, $\Delta\gamma = 5°$
Curl parameter $k_{v,\mathrm{curl}}$	5	$\{2, 3, 4, 5\}$
Radial spacing	16 m	–
Number of radial stations	24	–
Vortex-decay parameter $k_{\mathrm{VortexDecay}}$	0	–
Meandering constant C_{Meander}	2.1	–
Wake-filter cutoff frequency f_c	0.008 Hz	–

2.2.2. Reference FAST.Farm Wake-Model Parameterization

The reference FAST.Farm parameterization reported in Table 3 was adopted from published curled-wake studies and LES-oriented FAST.Farm calibrations for the IEA Wind 15 MW turbine rather than obtained through unrestricted calibration against the present farm-level cases. In particular, $k_{\mathrm{VortexDecay}}$ governs the downstream decay of the spanwise velocity components associated with the curled wake, whereas $k_{v,\mathrm{curl}}$ scales the eddy-viscosity-driven wake diffusion and therefore affects wake spreading and velocity-deficit recovery. The reference value $k_{v,\mathrm{curl}} = 5$ was retained for the yaw-misalignment sweep and for the subsequent four-turbine simulations, while the values reported in Table 3 were examined separately to characterize sensitivity to the modeled wake-recovery rate.

The wake-filter cutoff frequency was selected close to the VolturnUS-S surge natural frequency to avoid nonphysical overlap or overtaking of consecutively generated wake planes. This selection retains quasi-steady and sufficiently low-frequency effects associated with platform position and orientation while progressively attenuating higher-frequency wake pulsations caused by platform surge and pitch. The coupled platform, structural, hydrodynamic, and mooring responses remain resolved by OpenFAST because the filtering acts only on the rotor-level conditions supplied to the FAST.Farm wake-dynamics calculation. The selected cutoff frequency should therefore be regarded as a numerical modeling compromise for the present FAST.Farm formulation rather than as a generally calibrated value.

The sensitivity analysis was designed to distinguish the principal effects of the two investigated quantities: the imposed nacelle–yaw offset primarily controls wake-center displacement and yaw-sign asymmetry, whereas $k_{v,\mathrm{curl}}$ primarily modifies wake spreading, diffusion, and downstream velocity-deficit recovery. It was not intended to rank all FAST.Farm numerical, environmental, and controller uncertainties.

2.2.3. Wake-Field Extraction and Characterization Metrics

For each single-turbine case, FAST.Farm velocity fields were extracted on vertical planes at $x/D = 1$–4 and 6–10, where D is the rotor diameter, and post-processed using SAMWICH v0.1 [47].

Because the curled wake is generally asymmetric, the instantaneous wake center was recomputed from each velocity-field snapshot using the constant-area method implemented in SAMWICH [48], following its previous application to FAST.Farm curled-wake fields [23]. At downstream position x, the wake center is denoted by $\mathbf{r}_c(x,t) = [y_c(x,t), z_c(x,t)]^{\mathrm{T}}$. Its mean position and component-wise standard deviations are:

$$\bar{\boldsymbol{r}}_c(x) = \frac{1}{T_a}\int_{t_0}^{t_1} \boldsymbol{r}_c(x,t)\,\mathrm{d}t,$$
$$\sigma_{\xi_c}(x) = \left[\frac{1}{T_a}\int_{t_0}^{t_1} \left(\xi_c(x,t) - \bar{\xi}_c(x)\right)^2 \mathrm{d}t\right]^{1/2}, \qquad \xi \in \{y,z\}. \tag{3}$$

where $T_a = t_1 - t_0$. The mean lateral and vertical positions quantify wake deflection, while σ_{y_c} and σ_{z_c} quantify wake meandering. These quantities are normalized by D where appropriate.

Wake recovery and shape evolution are characterized using the normalized mean velocity deficit:

$$\delta_U(x,y,z) = \frac{U_\infty - \overline{U}(x,y,z)}{U_\infty}, \tag{4}$$

where U_∞ is the undisturbed hub-height wind speed and $\overline{U}$ is the time-averaged streamwise velocity. Lateral and vertical profiles through the mean wake center are used to evaluate wake displacement, spreading, asymmetry, and recovery.

2.3. Four-Turbine Coupled Wake-Steering Assessment

2.3.1. Reference Farm Layout and Operating Strategies

The coupled FAST.Farm assessment considered four IEA Wind 15 MW turbines mounted on VolturnUS-S platforms in a progressively staggered single-row layout. The turbine arrangement and numbering are illustrated in Figure 2. Turbines T1–T4 are numbered downstream, the x-axis is aligned with the nominal inflow at WD $= 0°$, and the y-axis is crosswind.

For turbine $i \in \{1,\ldots,4\}$, the undisplaced platform-reference coordinates are:

$$x_i = x_1 + (i-1)SD, \qquad y_i = y_c + \left(i - \frac{5}{2}\right)\frac{SD}{12}, \tag{5}$$

where $D = 240$ m, S is the streamwise spacing in rotor diameters, $x_1 = 300$ m, and $y_c = 0$. The FAST.Farm reference case uses $S = 7$, giving $\Delta x = 1680$ m and $\Delta y = 140$ m, with turbine coordinates $(x_i, y_i) = \{(300,-210),(1980,-70),(3660,70),(5340,210)\}$ m.

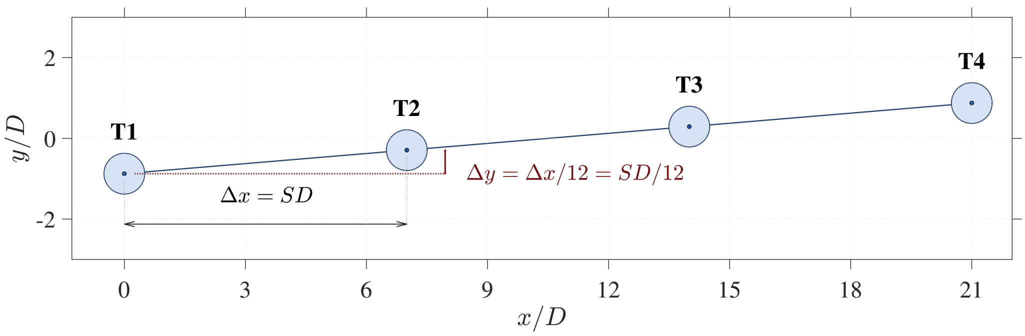

Figure 2. Four-turbine reference layout. The progressively staggered $S = 7$ configuration has streamwise and lateral separations of $7D$ and $0.583D$, respectively.

The layout is an idealized reference configuration intended to provide controlled wake interaction for coupled power- and load-response assessment. Comparable idealized floating arrays have been used in previous FAST.Farm studies [21,23]. Sensitivity to spacing and inflow conditions is examined separately using FLORIS, while longer-term aerodynamic relevance is assessed using the Tampen-derived layout.

Two operating strategies were evaluated using matched environmental realizations. Greedy operation used zero commanded yaw offset at all turbines. For static wake steering, FLORIS-derived offsets within $-20^\circ \leq \gamma_i^* \leq 20^\circ$ were applied to T1–T3, while T4 remained aligned because no modeled turbine was located downstream of it. The supervisory offsets remained constant during each statistical interval, while the ROSCO yaw controllers and floating-turbine dynamics remained active.

2.3.2. Static Yaw-Setpoint Generation and FLORIS-to-FAST.Farm Transfer

The simulation workflow evaluates the static wake-steering strategy using a multi-fidelity procedure. First, steady-state optimal yaw-offset setpoints are computed in FLORIS for each mean wind speed. These setpoints are then imposed in FAST.Farm through the ROSCO–ZeroMQ supervisory-control interface, where the coupled aero-hydro-servo-elastic response of the floating wind farm is evaluated, as illustrated in Figure 3. The comparison between the two operating strategies is therefore performed in FAST.Farm, while FLORIS is used only to generate the static yaw-offset commands.

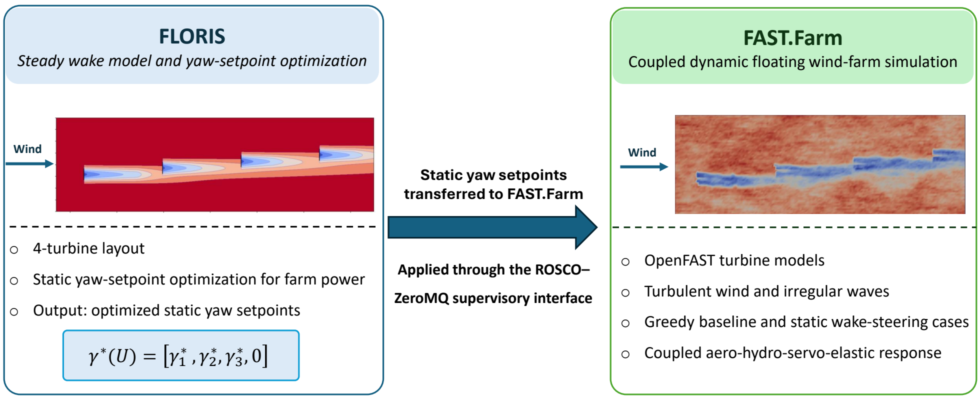

Figure 3. Multi-fidelity workflow for static wake-steering assessment. FLORIS is used to determine steady power-oriented yaw offsets, which are transferred through the ROSCO–ZeroMQ interface to FAST.Farm for coupled dynamic evaluation under turbulent wind and irregular waves.

The optimized yaw offsets imposed in the FAST.Farm simulations are summarized in Table 4. The same yaw-offset vector is applied to all three sea states for a given wind speed.

Table 4. FLORIS-derived yaw offsets imposed in FAST.Farm.

Wind Speed	T1	T2	T3	T4
7 m s^{-1}	13°	12°	10°	0°
8 m s^{-1}	13°	11°	10°	0°
9 m s^{-1}	14°	11°	9°	0°

Although both yaw signs were permitted within $-20^\circ \leq \gamma_i \leq 20^\circ$, the optimizer selected positive offsets for all controlled turbines. Under the adopted yaw-sign convention and staggered layout, these offsets displace the wakes away from the downstream rotors; their sign therefore results from the farm geometry and power objective rather than an imposed restriction. The yaw-sign asymmetry observed in the isolated single-turbine study does not by itself determine the farm-level optimum.

2.3.3. Environmental Conditions and FAST.Farm Simulation Matrix

The turbulent inflow was generated using a Kaimal spectrum with TI = 6% and a power-law shear exponent $\alpha = 0.06$ with Turbsim v2.00.07a-bjj Jonkman [49], consistent with the offshore measurements and profile relationships reported by Türk and Emeis [44], Jeans [45]. The investigated wind–wave conditions, operating strategies, number of realizations, simulation duration, and discarded transient are summarized in Table 5. For each wind–wave condition and turbulent-inflow realization, the same environmental realization was used for the greedy and wake-steering cases, enabling paired power and load comparisons. The complete matrix therefore comprises 90 coupled FAST.Farm simulations.

Table 5. Environmental conditions and operating strategies considered in the coupled FAST.Farm assessment.

Parameter	Label	Value
Mean wind speed at hub height	–	7, 8, and 9 $\mathrm{m\,s^{-1}}$
Sea state	Mild Medium Severe	$(H_s, T_p) = (1\,\mathrm{m}, 8\,\mathrm{s})$ $(H_s, T_p) = (4\,\mathrm{m}, 10\,\mathrm{s})$ $(H_s, T_p) = (8\,\mathrm{m}, 14\,\mathrm{s})$
wind–wave condition seeds	–	5
Control strategy	Greedy Static wake steering	Zero yaw offset Fixed optimized yaw offsets
Simulation duration Discarded transient	– –	4600 s per simulation First 1000 s

2.4. Complementary FLORIS-Based Aerodynamic Assessments

FLORIS was additionally used for a parametric aerodynamic sensitivity analysis of the four-turbine staggered layout and a resource-weighted annual energy-contribution assessment of a Tampen-derived 11-turbine layout. Both analyses used the fixed FLORIS configuration, turbine model, yaw constraints, zero-yaw reference, and serial-refine procedure described in Section 2.1.5. These extensions assess steady aerodynamic power only and do not extend the coupled FAST.Farm load conclusions to the additional operating conditions or layout.

2.4.1. Parametric Sensitivity Analysis of the Four-Turbine Staggered Layout

A systematic FLORIS analysis was performed to determine whether the predicted wake-steering benefit for the reference four-turbine case was specific to the selected turbine spacing and inflow condition. The sensitivity analysis used the parametric layout defined in Equation (5), with S varied over the investigated range. The parameter ranges, discretization intervals, reference condition, and yaw-angle constraints used in the FLORIS sensitivity analysis are summarized in Table 6.

Table 6. Parameter ranges and reference conditions used in the four-turbine FLORIS sensitivity analysis. The reference conditions correspond to the coupled FAST.Farm configuration.

Parameter	Symbol	Investigated Values	Reference Value
Layout spacing	S	$[6, 10]$, $\Delta(S) = 0.2$	7
Wind direction	WD	$[-17°, 10°]$, $\Delta WD = 1°$	0°
Hub-height wind speed	U	$[6, 10]\ \mathrm{m\,s^{-1}}$, $\Delta U = 0.2\ \mathrm{m\,s^{-1}}$	7, 8, 9 $\mathrm{m\,s^{-1}}$
Ambient turbulence intensity	TI	$[4\%, 8\%]$, $\Delta\mathrm{TI} = 0.2$ percentage points	6%
Yaw offsets of T1–T3	γ_i	$[-20°, 20°]$	Optimized
Yaw offset of T4	γ_4	Fixed	0°

Varying S scales both consecutive turbine separations according to $\Delta x = SD$ and $\Delta y = SD/12$, thereby preserving the stagger ratio $\Delta y/\Delta x = 1/12$. The analysis therefore examines a family of geometrically similar staggered layouts rather than varying streamwise spacing independently while holding the lateral offset fixed.

For every combination of spacing, wind direction, wind speed, and ambient turbulence intensity, two operating strategies were evaluated. The reference strategy was greedy zero-yaw operation:

$$\gamma^{G} = [0^\circ,\ 0^\circ,\ 0^\circ,\ 0^\circ].$$

For the wake-steering strategy, the yaw offsets were optimized independently for each operating condition:

$$\gamma^{*}(U, WD, S, \mathrm{TI}) = \arg\max_{\gamma} P_{\mathrm{farm}}(U, WD, S, \mathrm{TI}, \gamma), \quad (6)$$

subject to the yaw-angle constraints reported in Table 6. Turbine T4 was kept aligned because it has no downstream turbine within the modeled array that could benefit from deflection of its wake. The serial-refine optimization was repeated at every point in the parametric matrix, rather than transferring the yaw vector obtained for the reference condition, because the wake-overlap pattern and corresponding optimal yaw settings vary with spacing, wind direction, wind speed, and turbulence intensity.

The absolute and relative farm-power changes were calculated as follows:

$$\Delta P_{\mathrm{abs}} = P_{\mathrm{farm}}^{\mathrm{WS}} - P_{\mathrm{farm}}^{\mathrm{G}}, \quad (7)$$

and

$$\Delta P_{\mathrm{rel}} = 100 \frac{P_{\mathrm{farm}}^{\mathrm{WS}} - P_{\mathrm{farm}}^{\mathrm{G}}}{P_{\mathrm{farm}}^{\mathrm{G}}}, \quad (8)$$

where the superscripts G and WS denote greedy zero-yaw operation and optimized wake steering, respectively. No separate no-wake reference was used; all reported changes are calculated relative to the corresponding greedy zero-yaw condition. The resulting power-gain matrix was used to quantify the sensitivity of the optimized aerodynamic benefit to the principal parameters governing wake overlap and wake recovery.

2.4.2. Resource-Weighted Annual Energy Assessment of the Tampen-Derived Layout

The long-term aerodynamic relevance of static wake steering was assessed using an 11-turbine layout derived from the Hywind Tampen geometry. The original turbine locations were retained but populated with IEA Wind 15 MW reference turbines with $D = 240$ m. The resulting configuration is therefore a hypothetical Tampen-derived layout and not a numerical representation of the operating Hywind Tampen farm. The wind resource and the corresponding Tampen-derived turbine layout are shown in Figure 4.

The wind resource was obtained from the NORA3 hindcast at 150 m over 2001–2020 and discretized into wind-speed and wind-direction bins of 0.1 $\mathrm{m\,s^{-1}}$ and 2°, respectively. The occurrence probability f_{jk} of each bin was calculated from its fraction of the valid observations.

Only nonzero-probability bins with $4 \le U_j \le 13\ \mathrm{m\,s^{-1}}$ were evaluated. The upper limit corresponds to the maximum wind speed supported by the available turbine power, thrust, and yaw-response tables. The wind distribution was not renormalized after applying this restriction; so, the reported values retain the actual annual-frequency contribution of the modeled interval.

For each resource bin, FLORIS farm power was evaluated under zero-yaw operation and after independent serial-refine yaw optimization. For operating strategy c, the annual energy contribution over the modeled wind-speed interval was calculated as follows:

$$E^{c}_{4-13} = 8760 \sum_{\substack{j:\\ 4\le U_j\le 13}} \sum_{k} f_{jk} P^{c}_{jk}, \qquad c \in \{\mathrm{ZY}, \mathrm{WS}\}, \tag{9}$$

where P^{c}_{jk} is the corresponding farm power for wind-speed bin j, wind-direction bin k, and operating strategy c. The absolute and relative energy increases were defined as $\Delta E_{4-13} = E^{\mathrm{WS}}_{4-13} - E^{\mathrm{ZY}}_{4-13}$ and $\Delta E^{\mathrm{rel}}_{4-13} = 100\,\Delta E_{4-13}/E^{\mathrm{ZY}}_{4-13}$, respectively.

Because no FLORIS calculation or yaw optimization was performed above 13 $\mathrm{m\,s^{-1}}$, the reported quantities represent annual energy contributions over 4–13 $\mathrm{m\,s^{-1}}$, not complete full-operating-range annual energy production. No wake-steering benefit is inferred outside the modeled interval.

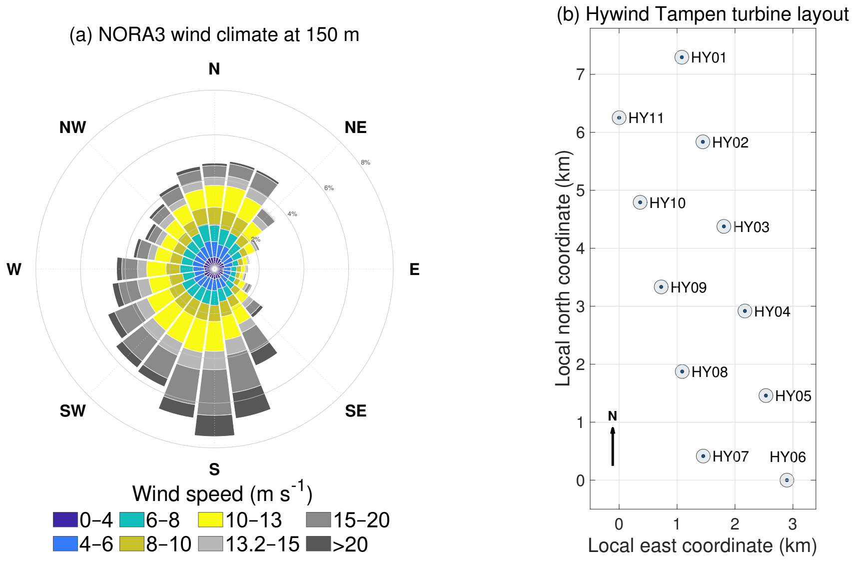

Figure 4. Inputs to the Tampen-derived resource-weighted annual energy-contribution assessment. Panel (**a**) shows the NORA3 wind climate at 150 m, and panel (**b**) shows the 11-turbine layout populated with IEA Wind 15 MW turbines.

2.5. FAST.Farm Performance Metrics and Post-Processing

2.5.1. FAST.Farm Power Metrics and Paired Statistical Treatment

For each wind-speed, sea-state, and turbulent-inflow realization, the static wake-steering case was compared with the corresponding greedy case generated using the same environmental realization. All power– and fatigue–load metrics were evaluated over the final 3600 s analysis interval after removal of the initial transient.

The mean generator power of turbine i under operating strategy c and turbulent-inflow realization s was calculated as follows:

$$\overline{P}^{c}_{i,s} = \frac{1}{T_{\mathrm{a}}}\int_{t_0}^{t_1} P^{c}_{i,s}(t)\,\mathrm{d}t, \qquad \overline{P}^{c}_{\mathrm{farm},s} = \sum_{i=1}^{N_{\mathrm{T}}} \overline{P}^{c}_{i,s}, \qquad T_{\mathrm{a}} = 3600\ \mathrm{s}, \quad N_{\mathrm{T}} = 4, \tag{10}$$

where $c \in \{\mathrm{G}, \mathrm{WS}\}$ denotes greedy and static wake-steering operation, respectively.

For any response quantity X, the paired relative and absolute changes for realization s were defined as follows:

$$q_{X,s} = 100\frac{X^{\mathrm{WS}}_{s} - X^{\mathrm{G}}_{s}}{X^{\mathrm{G}}_{s}}, \qquad \Delta X^{\mathrm{abs}}_{s} = X^{\mathrm{WS}}_{s} - X^{\mathrm{G}}_{s}. \tag{11}$$

For the power analysis, X represents either the farm-mean power or the mean power of an individual turbine. Positive values indicate an increase under static wake steering, whereas negative values indicate a reduction relative to the matched greedy case. The turbine-level changes are used to quantify the redistribution of power along the array.

For each operating condition, the paired mean and corresponding 95% confidence interval were calculated as follows:

$$\overline{q}_X = \frac{1}{N_s}\sum_{s=1}^{N_s} q_{X,s}, \qquad \mathrm{CI}_{95\%} = \overline{q}_X \pm t_{0.975,N_s-1}\frac{s_{q_X}}{\sqrt{N_s}}, \qquad N_s = 5, \tag{12}$$

where s_{q_X} is the sample standard deviation of the five paired changes. Unless otherwise stated, relative changes are reported as $\overline{q}_X$ with the corresponding 95% confidence interval, while strategy-specific absolute quantities are reported as the sample mean with ±1 sample standard deviation. Because only five matched realizations were available, the confidence intervals quantify seed-to-seed uncertainty and are not interpreted as evidence of complete statistical convergence.

2.5.2. Damage-Equivalent-Load and Power–Load Trade-Off Metrics

Fatigue loading was evaluated over the same 3600 s analysis interval using rainflow counting. For load channel k, turbine i, operating strategy c, and realization s, the damage-equivalent load was calculated as follows:

$$\mathrm{DEL}^{c}_{k,i,s} = \left[\frac{\sum_{j=1}^{N_{\mathrm{cyc}}} n_j\left(\Delta L_j\right)^{m_k}}{N_{\mathrm{eq}}}\right]^{1/m_k}, \tag{13}$$

where ΔL_j and n_j are the range and occurrence count of rainflow cycle j, m_k is the fatigue exponent associated with load channel k, and N_{eq} is the reference number of equivalent cycles. Identical fatigue-analysis settings were applied to the matched greedy and static wake-steering simulations. The evaluated responses were the blade-root resultant moment, tower-base resultant moment, yaw-bearing resultant moment, and FairTen1 tension.

Turbine-level relative DEL changes were calculated using Equation (11) with $X = \mathrm{DEL}_{k,i,s}$. Positive values indicate an increase under static wake steering, whereas negative values indicate a reduction relative to the matched greedy case.

For the farm-mean DEL, the absolute turbine DELs were first averaged separately for each strategy and matched realization, after which the paired relative change was calculated:

$$\overline{\mathrm{DEL}}^{c}_{k,s} = \frac{1}{N_{\mathrm{T}}}\sum_{i=1}^{N_{\mathrm{T}}} \mathrm{DEL}^{c}_{k,i,s}, \qquad q^{\mathrm{FM}}_{k,s} = 100\,\frac{\overline{\mathrm{DEL}}^{\mathrm{WS}}_{k,s} - \overline{\mathrm{DEL}}^{\mathrm{G}}_{k,s}}{\overline{\mathrm{DEL}}^{\mathrm{G}}_{k,s}}. \tag{14}$$

This quantity differs from the arithmetic mean of the four turbine-level percentage changes because the turbine DELs are averaged before normalization.

For the power–load trade-off, the maximum numerical turbine-level DEL change was selected separately within each realization:

$$q^{\mathrm{WT}}_{k,s} = \max_{i\in\{1,\ldots,N_{\mathrm{T}}\}}\left[100\,\frac{\mathrm{DEL}^{\mathrm{WS}}_{k,i,s} - \mathrm{DEL}^{\mathrm{G}}_{k,i,s}}{\mathrm{DEL}^{\mathrm{G}}_{k,i,s}}\right]. \tag{15}$$

The turbine defining $q^{\mathrm{WT}}_{k,s}$ may differ among realizations. The seed-wise values were summarized using Equation (12) and compared with the corresponding paired farm-power gain. The resulting metric therefore represents the mean of the seed-wise maximum numerical DEL changes rather than the response of a predetermined turbine or a farm-averaged load.

The reported DELs are comparative fatigue indicators for the simulated operating conditions and do not represent cumulative lifetime damage or remaining component service life.

2.5.3. Spectral Analysis

Power spectral densities were estimated from the detrended load signals using Welch's method, with identical sampling frequency, window, segment length, overlap, and frequency resolution for the matched greedy and wake-steering cases. The analysis focused on the yaw-bearing and tower-base moments to identify the frequency ranges associated with the corresponding DEL changes. The spectra were used only to interpret the frequency content of the load response; fatigue comparisons were based on the rainflow-counted DEL metrics.

3. Results

3.1. Single-Turbine FAST.Farm Wake Characterization

Figure 5 illustrates the wake-center extraction procedure used in the sensitivity analysis. For each velocity snapshot obtained from FAST.Farm, SAMWICH is used to identify the instantaneous wake outline and the corresponding wake center. The resulting wake-center time series is then reduced to two statistics: the mean wake-center position, used to quantify wake deflection, and the standard deviation of the wake-center motion, used to quantify wake meandering.

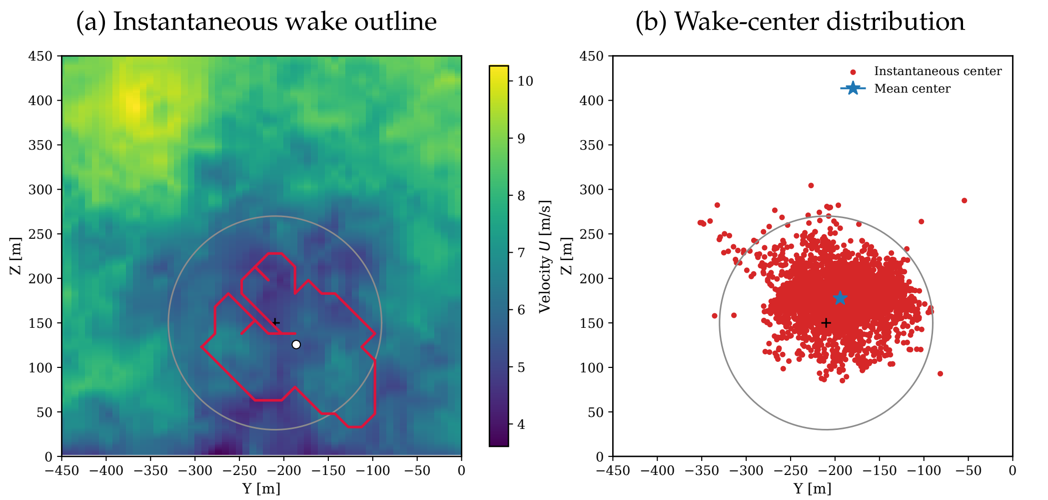

Figure 5. Wake-center extraction using SAMWICH for a representative plane located $6D$ downstream of the rotor. (**a**) Instantaneous velocity field on the YZ plane. The red contour denotes the SAMWICH constant-area wake outline used to identify the instantaneous wake center, shown by the white marker. (**b**) Distribution of instantaneous wake-center locations over the analyzed time window.

3.1.1. Yaw-Misalignment Sensitivity

Figure 6 compares the wake-center statistics and normalized deficit profiles across the downstream sampling planes for different imposed yaw angles. The near wake, up to approximately $4D$, is relatively insensitive to yaw variation, except for the larger yaw-misalignment cases. In contrast, the far wake, from $(6D)$ to $(10D)$, exhibits clearer separation between cases and is therefore more informative for assessing yaw-induced wake-trajectory changes.

The prescribed yaw offset has a clear impact on the wake trajectory. In Figure 6, cases with the same absolute value of γ are plotted using the same color, while the line style distinguishes the sign of the yaw angle: dashed lines correspond to negative yaw angles and solid lines correspond to positive yaw angles. This representation enables a direct comparison between $+\gamma$ and $-\gamma$ cases and highlights the asymmetry of the wake response.

Differences between yaw cases are already visible in the near wake, but they become much more pronounced farther downstream, where wake-center displacement accumulates and wake meandering increases. The deficit profiles indicate that yaw misalignment primarily shifts and broadens the wake, while its influence on the peak deficit is secondary compared with its effect on wake position.

The results reveal a clear asymmetry with respect to the sign of the yaw angle. Negative yaw cases show a stronger sensitivity than positive yaw cases of the same magnitude. As the magnitude of negative yaw increases, the wake deflection increases more noticeably, whereas the positive yaw cases exhibit a weaker variation with yaw angle. This yaw-sign asymmetry is particularly evident in the far-wake vertical-deflection response, even though the overall lateral wake-center displacement remains larger in magnitude.

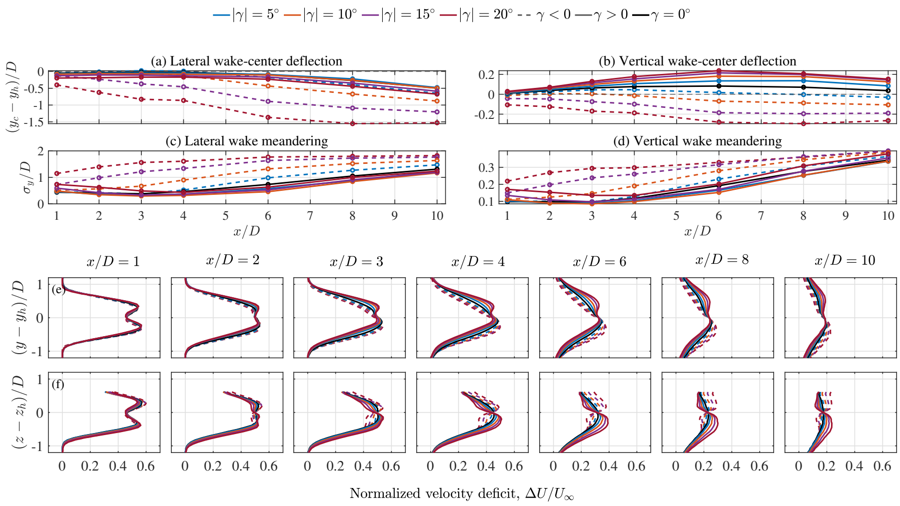

Figure 6. Yaw-angle sensitivity of the wake response. Panels (**a**–**d**) show lateral deflection, vertical deflection, lateral meandering, and vertical meandering, respectively; rows (**e**,**f**) show the corresponding lateral and vertical normalized velocity-deficit profiles at the indicated downstream locations.

3.1.2. Sensitivity to the Wake-Diffusion Parameter

Additional sensitivity tests were also performed for wake-model parameters such as $k_{v,\mathrm{curl}}$. These tests indicated that $k_{v,\mathrm{curl}}$ mainly affects wake spreading and downstream recovery rather than producing the strong wake-center displacement observed under yaw misalignment. The corresponding sensitivity results are shown in Figure 7.

Overall, the yaw sweep shows that the wake response is not symmetric with respect to the sign of γ. The far-wake planes provide the clearest evidence of this behavior, making them more suitable than the near-wake planes for evaluating yaw-induced wake deflection and meandering.

In both sensitivity studies, the floating-platform degrees of freedom remained active. The extracted wake-center trajectories therefore include the dynamically calculated rotor translations and rotations caused by platform motion, in addition to the imposed yaw-angle or wake-model-parameter variation. Platform motions were not prescribed independently.

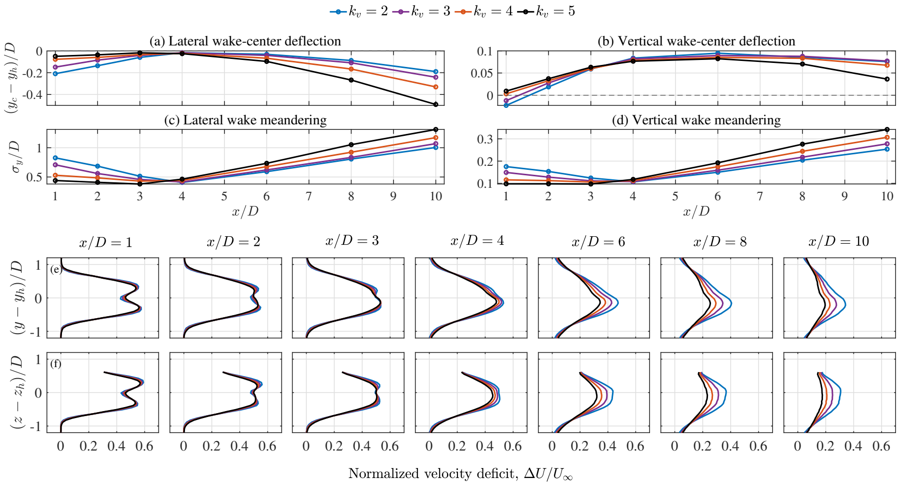

Figure 7. Sensitivity of the wake response to $k_{v,\mathrm{curl}}$. Panels (**a**–**d**) show lateral deflection, vertical deflection, lateral meandering, and vertical meandering, respectively; rows (**e**,**f**) show the corresponding lateral and vertical normalized velocity-deficit profiles at the indicated downstream locations.

3.2. Four-Turbine Wake-Steering Performance and Sensitivity

3.2.1. Farm-Level Power and Cross-Model Consistency

Table 7 reports the absolute farm power under greedy and static wake-steering operation, together with the paired absolute and relative power changes. Static wake steering increases the mean farm power under all nine investigated wind-speed and sea-state conditions. The relative gains range from approximately 4.05% to 5.18%, while the corresponding absolute increases range from approximately 0.63 to 1.07 MW.

Table 7. FAST.Farm farm-level power results. Values are means over five matched realizations; uncertainty statistics are based on the paired relative power changes.

U [m s^{-1}]	Sea State	P^{G}_{farm} [MW]	P^{WS}_{farm} [MW]	ΔP_{abs} [MW]	ΔP_{rel} [%], Mean ± SD	95% CI [%]
7	Mild	12.166	12.797	0.631	5.185 ± 0.101	[5.059, 5.311]
7	Medium	12.267	12.894	0.627	5.111 ± 0.117	[4.965, 5.257]
7	Severe	12.448	13.088	0.640	5.141 ± 0.118	[4.994, 5.288]
8	Mild	18.118	19.033	0.914	5.046 ± 0.055	[4.979, 5.114]
8	Medium	18.241	19.151	0.911	4.993 ± 0.053	[4.927, 5.058]
8	Severe	18.463	19.398	0.934	5.061 ± 0.023	[5.033, 5.089]
9	Mild	25.869	26.928	1.059	4.095 ± 0.030	[4.058, 4.132]
9	Medium	26.022	27.077	1.054	4.051 ± 0.036	[4.007, 4.096]
9	Severe	26.346	27.418	1.072	4.069 ± 0.063	[3.991, 4.147]

The influence of sea state on the relative power benefit is small. At a given wind speed, the difference among the mild, medium, and severe sea states is substantially smaller than the reduction in relative gain observed between 8 and 9 m s^{-1}. The dominant trend is therefore a decrease in the relative wake-steering benefit as wind speed increases within the investigated below-rated range. In absolute terms, however, the power increase becomes larger with wind speed because the baseline farm power also increases.

The paired-seed sample standard deviations are small, ranging from approximately 0.02 to 0.12 percentage points. Moreover, the lower bound of the 95% confidence interval remains above zero for every investigated condition. The positive farm-power gain is consistent across the matched turbulent-inflow realizations, and the corresponding 95%

confidence interval excludes zero for every investigated condition. Nevertheless, the confidence intervals quantify seed-to-seed uncertainty for the investigated cases and should not be interpreted as evidence of complete statistical convergence.

The comparison is intended to examine the consistency of the steady-state setpoint-generation model and the coupled dynamic model when the same yaw vectors are imposed. It is not treated as an independent validation exercise because both models remain numerical representations and no field, experimental, or independently resolved high-fidelity reference is introduced. The principal FAST.Farm result is therefore the retained farm-power response and the associated coupled load redistribution after transfer of the FLORIS-derived setpoints.

3.2.2. Turbine-Level Power Redistribution

Figure 8 compares the turbine- and farm-level relative power changes predicted by FLORIS and FAST.Farm. The farm-level benefit results from a redistribution of power along the array rather than from an increase at every turbine. The sea-state-specific FAST.Farm changes have the same sign and exhibit only limited variation at each wind speed. Therefore, for each matched turbulent-inflow realization, the relative changes obtained under the mild, medium, and severe sea states are first averaged before the mean and 95% confidence interval are calculated across the five realizations. The corresponding sea-state-averaged absolute turbine powers are reported in Table 8.

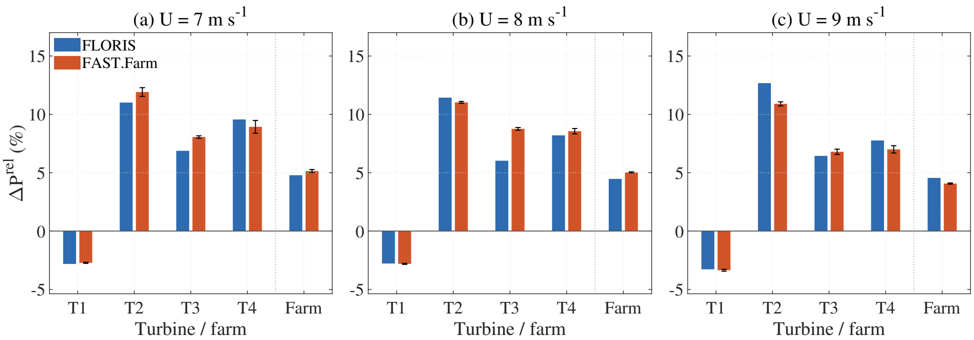

Figure 8. Turbine- and farm-level relative power changes. Panels (**a**–**c**) correspond to $U = 7$, 8, and 9 $\mathrm{m\,s^{-1}}$, respectively. FAST.Farm error bars show paired 95% confidence intervals; FLORIS results are deterministic imposed-yaw predictions.

Both models predict the same fundamental power-redistribution mechanism. The intentionally yawed upstream turbine T1 experiences a local power reduction, whereas the downstream turbines gain power because of reduced wake overlap. In FAST.Farm, the relative T1 power reductions are approximately 2.7%, 2.8%, and 3.4% at 7, 8, and 9 $\mathrm{m\,s^{-1}}$, respectively. These changes correspond to absolute reductions of 0.120, 0.184, and 0.310 MW.

T2 exhibits the largest relative increase, with gains of approximately 11.9%, 11.0%, and 10.9% at 7, 8, and 9 $\mathrm{m\,s^{-1}}$, respectively. The corresponding absolute increases are 0.296, 0.411, and 0.577 MW. The relative gains at T3 are approximately 8.1%, 8.8%, and 6.8%, corresponding to absolute increases of 0.220, 0.348, and 0.399 MW. At T4, the relative gains are approximately 8.9%, 8.6%, and 7.0%, with corresponding absolute increases of 0.237, 0.345, and 0.396 MW.

The relative gains of T3 and T4 decrease at 9 $\mathrm{m\,s^{-1}}$, consistent with the smaller farm-level relative benefit at this wind speed. In absolute terms, however, the downstream power recovery increases with wind speed because the baseline turbine-power level also increases. The 95% confidence intervals in Figure 8 remain narrow relative to the mean turbine-level changes, indicating that the direction and magnitude of the power redistribution are consistent across the five matched turbulent-inflow realizations.

Table 8. Sea-state-averaged turbine-level power balance. Values are means over the five matched realizations.

U [m s^{-1}]	Turbine	P_i^{G} [MW]	P_i^{WS} [MW]	ΔP_i^{abs} [MW]
7	T1	4.425	4.305	−0.120
7	T2	2.484	2.780	+0.296
7	T3	2.735	2.956	+0.220
7	T4	2.649	2.886	+0.237
8	T1	6.548	6.365	−0.184
8	T2	3.731	4.142	+0.411
8	T3	3.967	4.315	+0.348
8	T4	4.027	4.372	+0.345
9	T1	9.256	8.946	−0.310
9	T2	5.298	5.875	+0.577
9	T3	5.871	6.270	+0.399
9	T4	5.654	6.050	+0.396

At the farm level, FAST.Farm predicts relative gains of 5.15%, 5.03%, and 4.07% at 7, 8, and 9 m s^{-1}, respectively, compared with 4.79%, 4.47%, and 4.56% from FLORIS. Thus, the FAST.Farm prediction exceeds the FLORIS value by approximately 0.36 and 0.56 percentage points at 7 and 8 m s^{-1}, respectively. At 9 m s^{-1}, FLORIS predicts a gain approximately 0.48 percentage points larger than FAST.Farm. The maximum farm-level discrepancy between the two models is therefore approximately 0.56 percentage points. Despite model-dependent differences in the turbine-level redistribution, both models predict a positive net farm-power benefit at all three wind speeds.

The absolute power balance confirms that the net farm-level increase is generated by downstream power recovery. The combined gains of T2–T4 are 0.753, 1.104, and 1.372 MW at 7, 8, and 9 m s^{-1}, respectively. After accounting for the corresponding T1 losses, the resulting net farm-power increases are 0.633, 0.920, and 1.062 MW. Thus, although the relative farm-level gain decreases at 9 m s^{-1}, the absolute recovered power increases over the investigated wind-speed interval.

3.2.3. FLORIS Parametric Sensitivity

Having compared the imposed-yaw FLORIS and FAST.Farm responses at the three reference wind speeds, the independently reoptimized FLORIS analysis is used to examine the broader aerodynamic sensitivity of the optimized farm-power gain. Figures 9 and 10 present the six pairwise slices defined in Section 2.4.1, with the unplotted variables maintained at the corresponding reference values reported in Table 6.

Directional Robustness of the Transferred Yaw Vector

To distinguish the directional robustness of the yaw schedule transferred to FAST.Farm from the aerodynamic benefit available after condition-specific reoptimization, an additional fixed-yaw wind-direction slice was evaluated at $S = 7$, $U = 8$ m s^{-1}, and TI = 6%. At $WD = 0°$, the transferred yaw vector increases the FLORIS farm power by 4.47%, corresponding to 0.823 MW. Its maximum increase over the investigated directional interval is 5.25%, or 0.863 MW, at $WD = -2°$. The gain decreases to zero at $WD = +9°$, where the greedy and fixed-yaw solutions both produce approximately 25.838 MW. The transferred vector is therefore beneficial over only part of the investigated directional interval, demonstrating that a practical supervisory controller must update the yaw schedule as the filtered mean wind direction changes.

Spacing-Dependent Response

Figure 9 presents the three pairwise sensitivities involving the layout-spacing parameter. The spacing–wind-direction map in Figure 9a exhibits the largest variation. The optimized gain is concentrated in two directional regions, one close to $WD = 0°$ and another approximately between $WD = -8°$ and $-10°$, where the rotated inflow produces substantial wake interaction within the staggered turbine row. The gain approaches zero at directions for which the downstream turbines experience limited wake overlap.

The directional response is non-monotonic, with the two high-gain regions separated by a comparatively low-gain band near $WD = -5°$. This structure reflects changes in the wake-interaction topology as the inflow rotates relative to the staggered layout: relatively small directional changes can modify which downstream turbines are intercepted by the wakes of the upstream machines and therefore alter the power recoverable through yaw-based wake redirection.

Within the favorable directional regions, the optimized relative gain decreases systematically as the layout spacing increases. At smaller spacings, the zero-yaw configuration produces stronger turbine-to-turbine wake interactions and therefore provides greater potential for wake steering to redistribute the available wind resource. As the spacing increases, natural wake recovery reduces the difference between zero-yaw and optimized operation. At $WD = 0°$, $U = 8\ \mathrm{m\,s^{-1}}$, and TI = 6%, the optimized gains at $S = 6, 7, 8, 9$, and 10 are 8.3%, 4.5%, 2.9%, 1.3%, and 0.5%, respectively, corresponding to a decrease of 7.8 percentage points from $6D$ to $10D$.

Figure 9b shows that increasing ambient turbulence intensity also reduces the optimized gain, particularly at smaller spacings where the initial zero-yaw wake losses are strongest. At larger spacings, the gain is already comparatively limited and its additional sensitivity to turbulence intensity becomes weaker.

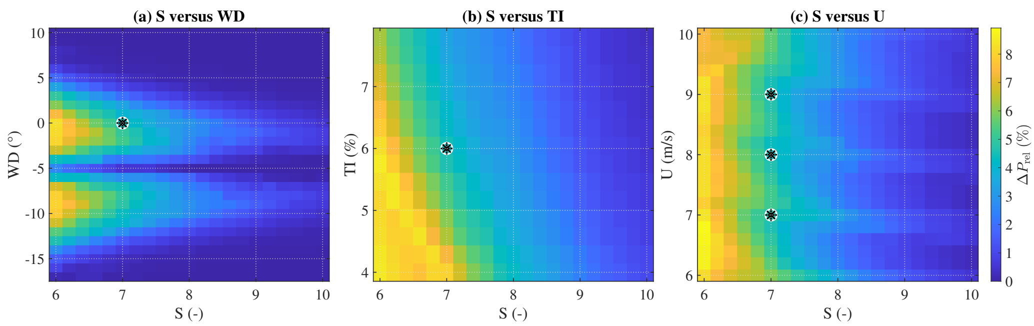

Figure 9. Spacing-dependent FLORIS sensitivity of the optimized farm-power gain. Panel (**a**) shows the relative farm-power gain as a function of turbine spacing and wind direction at $U = 8\ \mathrm{m\,s^{-1}}$ and TI = 6%. Panel (**b**) shows the sensitivity to turbine spacing and ambient turbulence intensity at $U = 8\ \mathrm{m\,s^{-1}}$ and $WD = 0°$, while panel (**c**) shows the sensitivity to turbine spacing and wind speed at $WD = 0°$ and TI = 6%. Stars identify the FAST.Farm reference conditions: panels (**a**,**b**) contain the $S = 7$ reference condition, whereas panel (**c**) contains the three simulated wind speeds of 7, 8, and 9 $\mathrm{m\,s^{-1}}$ at $S = 7$.

The spacing–wind-speed response in Figure 9c confirms that spacing produces the dominant variation along this slice. At the reference spacing $S = 7$, the independently reoptimized FLORIS gains are approximately 5.27%, 4.50%, and 4.81% at 7, 8, and 9 $\mathrm{m\,s^{-1}}$, respectively. The relative gain therefore varies moderately with wind speed, decreasing from 7 to 8 $\mathrm{m\,s^{-1}}$ and increasing slightly at 9 $\mathrm{m\,s^{-1}}$, while remaining below the 7 $\mathrm{m\,s^{-1}}$ value. In comparison, the reduction associated with increasing spacing is substantially larger. The reference condition lies within a continuous region of positive optimized gain rather than at an isolated optimum. The 4.50% result represents condition-specific FLORIS reoptimization at $U = 8\ \mathrm{m\,s^{-1}}$, whereas the 4.47% result reported above is obtained using the fixed yaw vector transferred to FAST.Farm.

Overall, the three spacing-dependent maps show that wake-interaction geometry, governed principally by wind direction and layout spacing, produces the largest changes in optimized aerodynamic benefit. Wind speed and ambient turbulence intensity provide secondary modulation within the investigated parameter ranges.

Environmental Response

Figure 10 presents the remaining environmental parameter combinations at the reference spacing. The wind-direction–turbulence-intensity map in Figure 10a retains the same two principal high-gain directional bands identified in the spacing–direction analysis. Increasing turbulence intensity generally reduces the peak gain but does not substantially shift the wind directions at which the largest gains occur. Wind direction therefore controls the wake-interaction geometry, whereas turbulence intensity mainly modifies the strength and downstream persistence of the wakes.

The wind-direction–wind-speed map in Figure 10b shows that the directional structure persists throughout the investigated 6–10 $\mathrm{m\,s^{-1}}$ range. The largest gains remain associated with the two strongly waked directional regions, while directions outside these regions exhibit only limited sensitivity to wind speed. At $WD = 0°$, the three FAST.Farm wind speeds lie within the same continuous positive-gain region, although the relative gain decreases slightly from 7 to 9 $\mathrm{m\,s^{-1}}$.

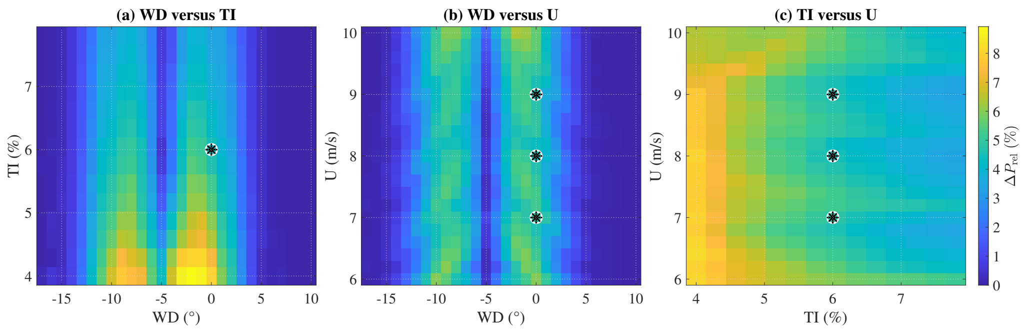

Figure 10. Environmental FLORIS sensitivity of the optimized farm-power gain. Panel (**a**) shows the relative farm-power gain as a function of wind direction and ambient turbulence intensity at $S = 7$ and $U = 8\ \mathrm{m\,s^{-1}}$. Panel (**b**) shows the sensitivity to wind direction and wind speed at $S = 7$ and TI = 6%, while panel (**c**) shows the sensitivity to turbulence intensity and wind speed at $S = 7$ and $WD = 0°$. Stars identify the FAST.Farm reference conditions: panel (**a**) contains the $U = 8\ \mathrm{m\,s^{-1}}$, $WD = 0°$, and TI = 6% condition, whereas panels (**b**,**c**) contain the three simulated wind speeds of 7, 8, and 9 $\mathrm{m\,s^{-1}}$.

In comparison, the turbulence-intensity–wind-speed map in Figure 10c varies smoothly. At the reference direction and spacing, the relative gain generally decreases as either wind speed or turbulence intensity increases. The combined influence of these two parameters is nevertheless weaker than the directional sensitivity observed in Figure 10a,b. This indicates that the optimized wake-steering benefit for the considered layout is governed primarily by wake overlap, which is controlled by wind direction and turbine spacing, while wind speed and turbulence intensity provide secondary modulation.

At the central reference condition, $S = 7$, $WD = 0°$, $U = 8\ \mathrm{m\,s^{-1}}$, and TI = 6%, FLORIS predicts an independently optimized gain of approximately 4.50%. This is approximately 0.49–0.56 percentage points lower than the 4.99–5.06% gain obtained from the coupled FAST.Farm simulations at 8 $\mathrm{m\,s^{-1}}$ across the three sea states. The two models nevertheless predict the same positive farm-power-benefit trend at the reference condition, while the FAST.Farm results additionally include turbulent-inflow variability, wave excitation, and structural dynamics.

Overall, the parametric sweep demonstrates that the selected FAST.Farm condition is representative of a broader region of positive wake-steering performance. The results also show that the magnitude of the benefit is highly configuration-dependent: gains approach 11–12% at the smallest investigated spacing and favorable inflow directions, but become small when the turbine spacing is large or when the inflow direction produces weak wake overlap.

3.2.4. Fatigue–Load Response

To distinguish aggregate load trends from localized turbine-level responses, the DEL results are presented at three complementary levels in Figure 11. First, the paired relative change in the farm-mean DEL is used to identify the overall response of each load component. Second, the FairTen1 response is examined at the turbine level to show how the station-keeping load is redistributed along the array. Finally, the farm-power gain is compared with the seed-wise worst-turbine DEL change to assess whether the positive power response is accompanied by localized fatigue–load penalties. In all cases, the statistical sample consists of the five matched turbulent-inflow realizations; the four turbines are not treated as independent realizations.

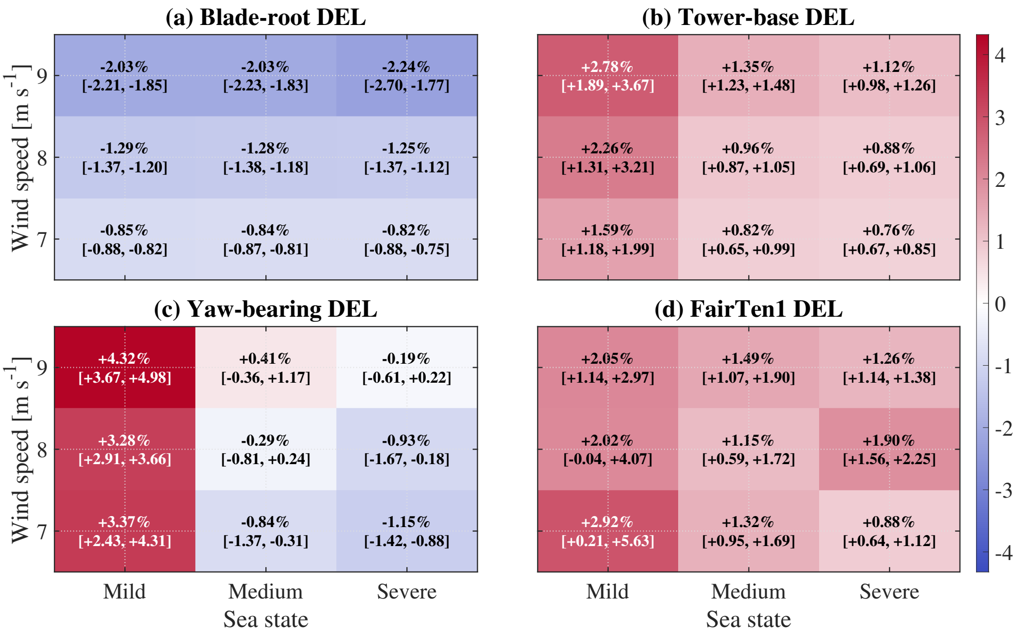

Figure 11. Farm-mean damage-equivalent-load changes. Panels (**a**–**d**) show the paired relative changes in blade-root, tower-base, yaw-bearing, and FairTen1 DEL, respectively. Cell text reports the mean and 95% confidence interval; complete statistics are provided in Table A1.

The blade-root DEL decreases under every investigated condition. The mean reduction increases in magnitude with wind speed, from approximately 0.82–0.85% at 7 $m\,s^{-1}$ to 1.25–1.29% at 8 $m\,s^{-1}$, and 2.03–2.24% at 9 $m\,s^{-1}$. All corresponding 95% confidence intervals remain below zero. This farm-mean reduction is consistent with the downstream relief associated with modified wake exposure exceeding the localized penalties when the four turbines are considered collectively.

The tower-base DEL exhibits the opposite farm-mean trend and increases under all nine wind–wave conditions. The increases range from 0.76% to 2.78%, with the largest response occurring under the mild sea state at 9 $m\,s^{-1}$. The larger increases under the mild sea state suggest that the relative influence of the wake-steering-induced aerodynamic redistribution is more visible when wave-induced loading is comparatively weak. Under medium and severe sea states, the relative increases are smaller, although their confidence intervals remain above zero. The tower-base response therefore reflects the combined influence of redistributed rotor thrust, tower loading, and low-frequency platform excitation rather than a uniform dependence on wave severity alone.

The yaw-bearing response is the most condition-dependent. Under the mild sea state, the farm-mean DEL increases by 3.28–4.32%, and the corresponding confidence intervals remain above zero. In contrast, reductions are obtained at 7 and 8 $\mathrm{m\,s^{-1}}$ under the severe sea state and at 7 $\mathrm{m\,s^{-1}}$ under the medium sea state. The confidence interval crosses zero for the medium-sea cases at 8 and 9 $\mathrm{m\,s^{-1}}$ and for the severe-sea case at 9 $\mathrm{m\,s^{-1}}$, indicating that the direction of the farm-mean response is not clearly resolved across the five available realizations for these conditions. This mixed behavior is consistent with the yaw bearing being affected by both intentional rotor–wind misalignment and the sea-state-dependent floating-platform response.

The farm-mean FairTen1 DEL increases under all investigated conditions, with mean changes between 0.88% and 2.92%. The largest mean increase and widest confidence interval occur at 7 $\mathrm{m\,s^{-1}}$ under the mild sea state. At 8 $\mathrm{m\,s^{-1}}$ under the mild sea state, the confidence interval extends slightly across zero, whereas the intervals for the remaining conditions remain above zero. The results indicate a modest overall increase in fairlead-tension cycling, but the turbine-level analysis presented subsequently shows that this farm-mean response can conceal substantially larger localized changes.

Overall, the heatmap demonstrates that static wake steering does not produce a uniform fatigue response. Blade-root loading improves at the farm-mean level, whereas tower-base and FairTen1 loading generally increase, and the yaw-bearing response changes sign with operating condition. The narrow confidence intervals observed for many conditions indicate consistent paired responses across the five available realizations, while the wider intervals for selected yaw-bearing and FairTen1 cases identify conditions for which seed-to-seed variability is more influential. Complete values are reported in Table A1.

The turbine-level extrema reported in Table A1 also show why the farm-mean response should not be interpreted as a uniform turbine-level effect. For example, although the farm-mean blade-root DEL decreases by 2.03–2.24% at 9 $\mathrm{m\,s^{-1}}$, T2 exhibits a mean increase of 0.70–1.46%, depending on sea state. Similarly, a negative farm-mean yaw-bearing change can coexist with a positive turbine-level penalty. At 8 $\mathrm{m\,s^{-1}}$ under the severe sea state, the farm-mean yaw-bearing DEL decreases by 0.93%, while the maximum turbine-level mean change is +1.10% at T4. These results confirm that farm-mean quantities can underrepresent localized fatigue penalties.

Figure 12 provides a more detailed view of the FairTen1 response at 7 $\mathrm{m\,s^{-1}}$. The absolute DEL levels increase substantially from the mild to the severe sea state, demonstrating that wave condition remains the dominant factor governing the overall magnitude of the fairlead-tension fatigue loading. The relative difference between greedy and static wake-steering operation, however, is not distributed uniformly among the four turbines.

T1 experiences a reduction in FairTen1 DEL under all three sea states. The mean reductions are approximately 3.5%, 1.8%, and 2.1% under the mild, medium, and severe sea states, respectively. This reduction is accompanied by increases at the downstream turbines, indicating that wake steering changes the distribution of aerodynamic thrust and the associated platform and mooring response along the array.

The largest localized response occurs at T2 under the mild sea state, where the mean FairTen1 DEL increases by 12.79%. This increase is substantially larger than the corresponding farm-mean change of 2.92%. The wider confidence interval at T2 also indicates stronger seed-to-seed sensitivity under this condition. Under the medium and severe sea states, the T2 increases are reduced to approximately 4.52% and 2.50%, respectively. T3 and T4 generally exhibit smaller positive changes, although the direction of the T3 response under the mild sea state is not clearly resolved because its confidence interval crosses zero.

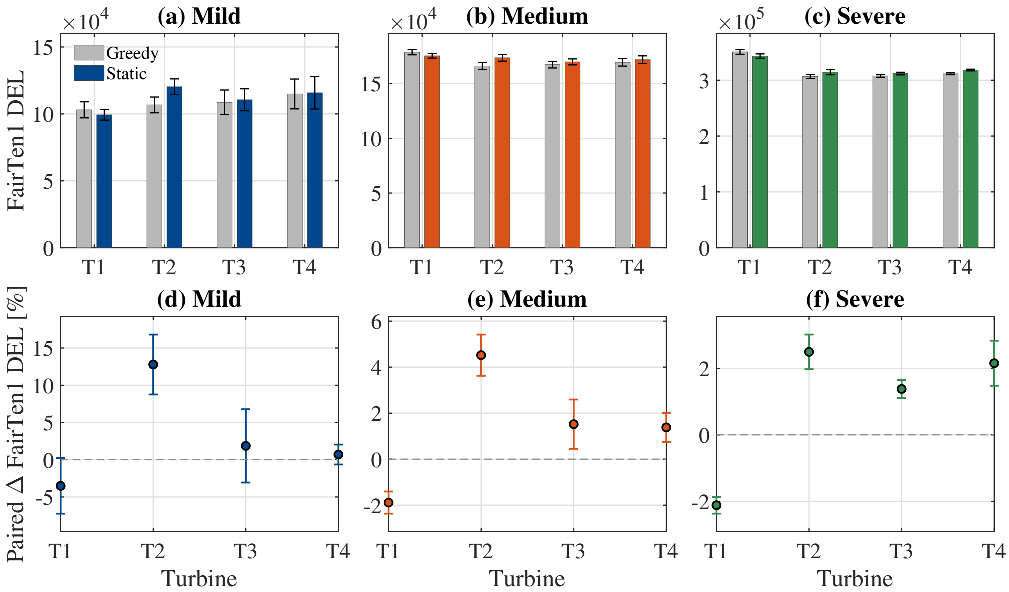

Figure 12. Turbine-level FairTen1 fatigue response at 7 m s^{-1}. Panels (**a**–**c**) show absolute DELs under greedy and static wake-steering operation, and panels (**d**–**f**) show the corresponding paired relative changes for the mild, medium, and severe sea states.

The contrast between the absolute and relative panels is important. The severe sea state produces the largest absolute FairTen1 DEL values, but the largest relative wake-steering penalty occurs under the mild sea state. This indicates that the wake-steering contribution is more prominent relative to the lower environmental baseline loading of the mild case. Under severe waves, the absolute mooring-line fatigue level is considerably greater, while the incremental relative effect of wake steering is smaller.

The turbine-level distribution therefore indicates that the modest farm-mean FairTen1 increase does not represent a uniform loading penalty across the array. Instead, the response consists of a reduction at T1 and localized increases downstream, particularly at T2. This redistribution is consistent with wake-steering-induced changes in rotor thrust, mean platform offset, and low-frequency platform motion. A complete causal separation of aerodynamic, hydrodynamic, and station-keeping contributions would require additional dedicated simulations and is not inferred from the DEL values alone.

Figure 13 combines the paired farm-power gain with the seed-wise worst-turbine DEL response. The horizontal confidence intervals are narrow and remain entirely within the positive power-gain region for all investigated wind–wave conditions. This confirms that the approximately 4–5% farm-power increase is consistent across the five matched realizations. The vertical responses are more component-dependent and, in several cases, exhibit substantially wider confidence intervals.

For the blade-root DEL, the worst-turbine response remains close to zero or below zero for most 7 and 8 m s^{-1} conditions, indicating that the farm-power benefit can be obtained without a clear localized blade-root penalty in these cases. At 9 m s^{-1}, however, the worst-turbine response becomes positive and reaches approximately 0.7–1.5%, despite the negative farm-mean blade-root changes shown in Figure 11. This again demonstrates that a favorable farm-mean result does not guarantee a reduction at every turbine.

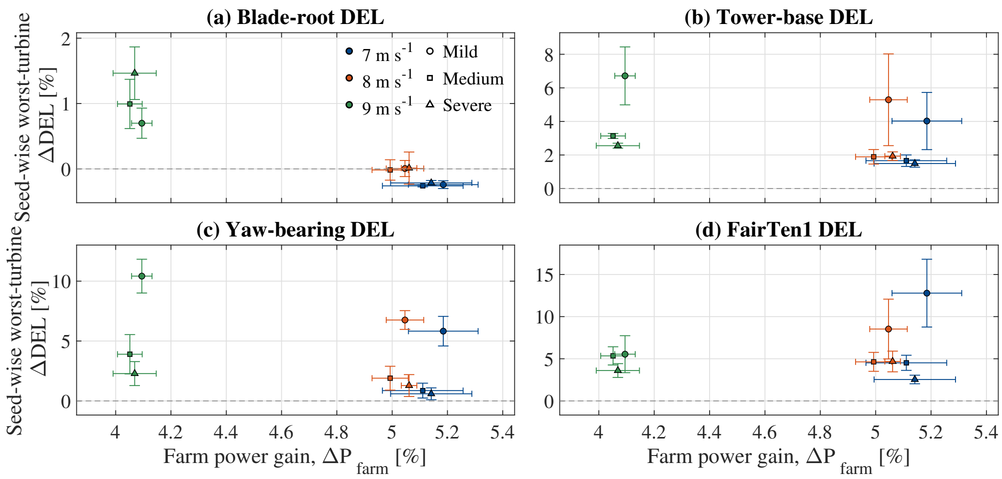

Figure 13. Power–load trade-off under static wake steering. Farm-power gain is compared with the seed-wise worst-turbine DEL change for (**a**) blade root, (**b**) tower base, (**c**) yaw bearing, and (**d**) FairTen1. Color denotes wind speed and marker shape denotes sea state.

The tower-base response is positive for every condition in the worst-turbine representation. The largest penalties occur under the mild sea state and increase with wind speed, reaching approximately 6.7% at 9 $\mathrm{m\,s^{-1}}$. The yaw-bearing response shows an even stronger localized penalty, with a maximum of approximately 10.4% at 9 $\mathrm{m\,s^{-1}}$ under the mild sea state. Positive worst-turbine yaw-bearing changes also occur for conditions where the farm-mean yaw-bearing DEL is negative or close to zero. Consequently, a farm-level or farm-mean assessment alone would not identify the full yaw-system loading implication.

FairTen1 exhibits the largest localized relative penalty in the investigated dataset. At 7 $\mathrm{m\,s^{-1}}$ under the mild sea state, the seed-wise worst-turbine mean reaches approximately 12.8%, while the paired farm-power gain remains approximately 5.1%. The large vertical confidence interval indicates that the magnitude of this localized response is sensitive to the turbulent realization, although its mean remains clearly positive. Under medium and severe sea states, the worst-turbine FairTen1 penalties are smaller but remain positive.

No monotonic relationship is observed between the magnitude of the farm-power gain and the localized DEL penalty. For example, the 9 $\mathrm{m\,s^{-1}}$ conditions produce the smallest relative farm-power gain, approximately 4.1%, but include the largest worst-turbine yaw-bearing response. Conversely, conditions with similar farm-power gains can exhibit substantially different tower-base, yaw-bearing, and FairTen1 penalties. The power gain alone is therefore not a sufficient indicator of the structural consequence of a wake-steering setpoint.

The trade-off results support the use of turbine- and component-specific load constraints in future wake-steering optimization. A practical supervisory controller should not maximize farm power independently of yaw-bearing, tower-base, and mooring-load responses. Instead, activation thresholds, directional sectors, sea-state information, and component-level fatigue constraints should be considered. The present intervals quantify uncertainty across the five available matched realizations, but they do not establish statistical convergence or long-term lifetime damage.

3.2.5. Spectral Interpretation of Load Changes

The DEL results indicate that the wake-steering control strategy affects the investigated load components differently. In particular, the yaw-bearing moment response is the most sensitive to the yaw control strategy, whereas the tower-base moment response shows a stronger dependence on wind speed and sea-state severity. To interpret these trends, PSD comparisons are used to identify the frequency ranges where the load's energy distribution differs with greedy and wake-steering controllers. The PSD analysis therefore provides a mechanism-oriented interpretation of the DEL variations observed in Figures 14 and 15.

Yaw-Bearing Response

As can be seen in Figure 14, wake-steering control does not uniformly increase the yaw-bearing moment response over the entire frequency range. For T1, the PSD is reduced between approximately 0.05 and 0.07 Hz. This interval is close to the platform heave natural frequency and overlaps the severe-sea-state wave-energy peak at approximately 0.071 Hz. At higher frequencies, however, the wake-steering control strategy increases the yaw-bearing moment PSD over much of the 0.08–0.70 Hz range. The strongest amplification occurs at the upstream yaw-controlled turbine T1, becomes progressively weaker at T2 and T3, and is almost absent at the non-yawed downstream turbine T4.

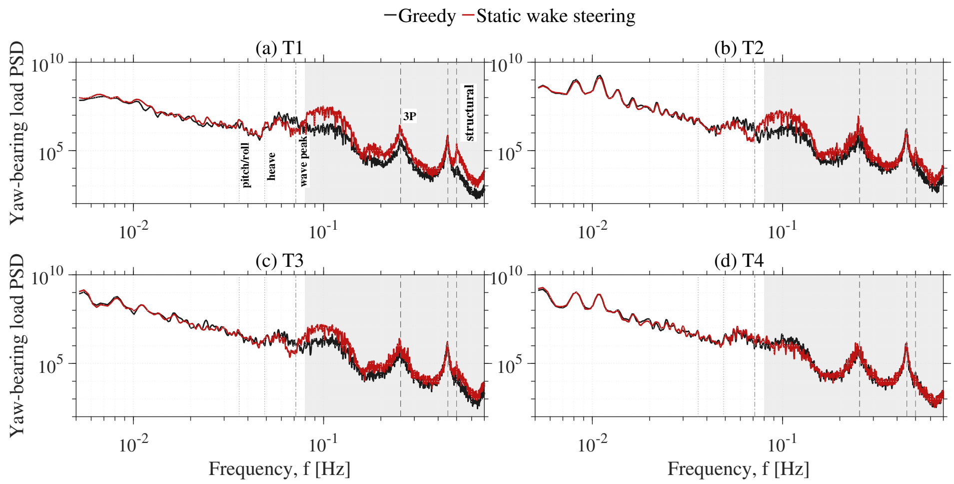

Figure 14. Yaw-bearing moment power-spectral densities. Panels (**a**–**d**) show turbines T1–T4 at 7 m s^{-1} under the severe sea state. Black and red curves denote greedy and static wake-steering operation, respectively; shaded and vertical reference lines identify the selected rotor, platform, and structural frequency ranges.

The peak near (0.25 Hz) is interpreted as the lower part of the 3P blade-passing frequency region, provided that the mean rotor speed in this case is close to (5 rpm). The responses observed between 0.45 and 0.50 Hz lie close to the first tower-bending modal range. The peak near 0.50 Hz is therefore consistent with the first fore-aft tower mode, while the response near 0.45 Hz may be associated with the side-to-side mode or with a broadened coupled tower response. Because the two tower modes are closely spaced and may be coupled under yawed and floating operation, they cannot be assigned unambiguously from the yaw-bearing moment PSD alone. Nevertheless, the additional amplification observed at T1 under the wake-steering strategy indicates that yaw misalignment increases the yaw-bearing moment spectra response within the first tower-bending frequency range.

The physical mechanism is associated with the asymmetric rotor loading introduced by yaw misalignment. The skewed inflow produces a nonuniform aerodynamic-load distribution over the rotor disk, and the rotation of the blades through this asymmetric flow periodically modulates the hub-force and yaw-moment components. These loads are transmitted through the nacelle and yaw bearing to the tower. When their spectral content overlaps the first tower-bending modes, the structural response can be amplified. The additional T1 response near 0.50 Hz under the wake-steering strategy therefore suggests that yaw misalignment enhances the coupling between rotor-induced loading and the first tower-bending response.

Tower-Base Response

To complement the yaw-bearing moment PSD analysis, the tower-base moment response is examined at 9 m s^{-1}, where the DEL results showed the clearest increase under the wake-steering strategy. The purpose of this comparison is to determine whether the tower-base moment increase is associated with a narrow or broader frequency range and whether this response changes with sea-state severity along the turbine row. At frequencies below approximately 0.04 Hz, the spectra for the three sea states are relatively similar. Beginning near 0.045 Hz, the medium- and severe-sea-state spectra become progressively larger than the mild-sea-state response, and the separation persists over a broad frequency interval extending to approximately 0.12 Hz.

This interval overlaps with the platform pitch/roll and heave natural-frequency range together with the wave-energy peaks of the investigated sea states. The tower-base response is therefore governed by the combined effects of hydrodynamic excitation, platform motion, aerodynamic thrust, and tower structural response. The broad spectral separation between sea states, rather than the presence of one isolated peak, indicates that the sea-state influence is distributed over a coupled low-frequency range.

Within each sea state, the greedy and static wake-steering curves remain comparatively close. The control-related changes are therefore more subtle than the differences produced by the changing sea state and are distributed over a broad frequency interval. This is consistent with the relatively modest farm-mean tower-base DEL increases of approximately 0.76–2.78%. Because a DEL integrates weighted cyclic content over frequency, small but persistent spectral differences can produce a measurable DEL increase even when no single controller-specific resonance dominates the spectrum.

A local minimum is visible near approximately 0.16–0.17 Hz for all turbines, sea states, and operating strategies. Because this feature occurs consistently in both the greedy and wake-steering responses, it is not interpreted as a consequence of the static yaw offsets.

The tower-base spectra therefore support a different interpretation from that obtained for the yaw-bearing moment. The yaw-bearing response shows clearer sensitivity to intentional yaw misalignment in the rotor and structural frequency ranges, whereas the tower-base response is dominated by low-frequency wave–platform dynamics, with the control strategy producing smaller modifications superimposed on the sea-state-dependent baseline. Consequently, the tower-base DEL increase should not be interpreted as a purely aerodynamic wake-steering effect; it reflects interaction among redistributed aerodynamic thrust, hydrodynamic excitation, floating-platform motion, and tower response.

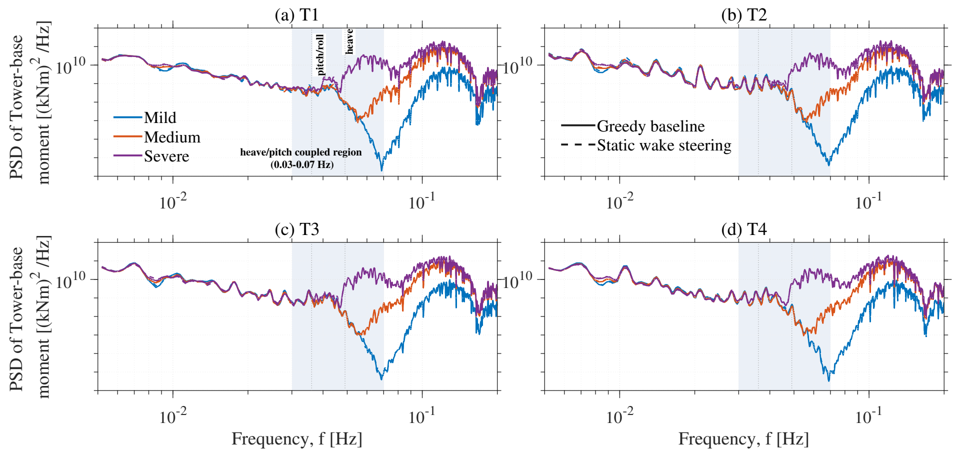

Figure 15. Tower-base resultant-moment power-spectral densities. Panels (**a**–**d**) show turbines T1–T4 at 9 m s^{-1}. Colors denote sea state, solid and dashed curves denote greedy and static wake-steering operation, and the shaded region identifies the platform pitch/heave frequency range.

3.3. Resource-Weighted Annual Energy-Contribution for the Tampen-Derived Layout

Over the modeled wind-speed interval of 4–13 $\mathrm{m\,s^{-1}}$, zero-yaw operation produced a resource-weighted annual energy contribution of 396.489 GWh $\mathrm{year^{-1}}$, whereas optimized static wake steering produced 400.142 GWh $\mathrm{year^{-1}}$. The corresponding increase was 3.653 GWh $\mathrm{year^{-1}}$, equivalent to 0.921% relative to the zero-yaw reference.

Figure 16 shows the contribution of each wind direction and wind-speed class to the annual energy increase. The largest contributions occur for winds approaching from approximately the north–northwest and south–southeast sectors. These directions are approximately aligned with the principal turbine rows of the Tampen-derived layout and therefore generate the strongest turbine-to-turbine wake interactions. Under these conditions, the zero-yaw farm experiences substantial wake overlap, providing the greatest opportunity for wake steering to increase downstream-turbine power production. Smaller, but still visible, contributions occur in the southwest, west, and northeast sectors, whereas directions with limited turbine alignment provide comparatively little annual benefit.

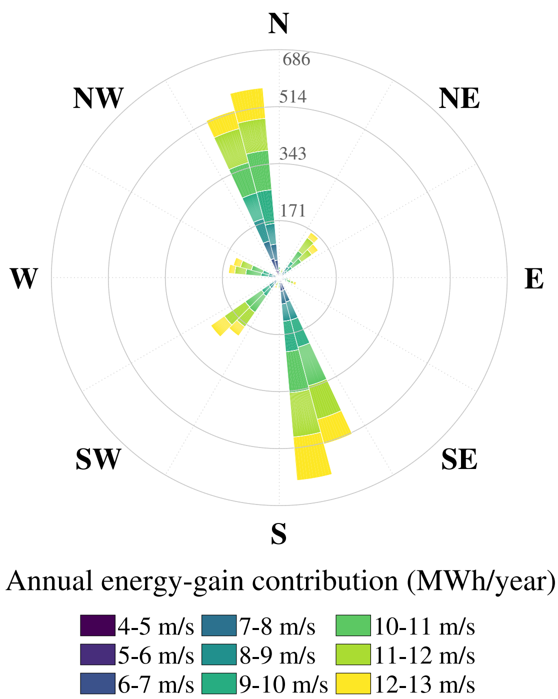

Figure 16. Resource-weighted annual energy-gain contribution for the Tampen-derived layout. Annual wake-steering energy-gain contribution for the Tampen-derived 11-turbine layout, resolved by meteorological wind direction and wind-speed class. The radial extent represents the resource-weighted annual energy increase relative to zero-yaw operation. Meteorological directions indicate the direction from which the wind approaches, with 0° corresponding to north and angles increasing clockwise. Contributions are evaluated over the modeled wind-speed range of 4–13 $\mathrm{m\,s^{-1}}$.

The largest contribution from an individual wind-direction sector occurred at 170°, where wake steering contributed 612.47 MWh $\mathrm{year^{-1}}$. When the contributions were aggregated by wind-speed class, the 10–11 $\mathrm{m\,s^{-1}}$ class provided the largest annual contribution of 799.20 MWh $\mathrm{year^{-1}}$. This result reflects the combined influence of occurrence probability, available aerodynamic power, and directional wake overlap in the Tampen-derived layout.

These quantities represent the annual energy contribution of the modeled 4–13 $\mathrm{m\,s^{-1}}$ interval. The wind distribution was not renormalized after restricting the modeled range, and no wake-steering gain was inferred outside this interval. The reported values should therefore not be interpreted as the complete full-operating-range AEP of either the operating Hywind Tampen farm or the hypothetical Tampen-derived 15 MW layout.

4. Discussion

4.1. Transferability and Aerodynamic Generalization

The coupled simulations demonstrate that the power-oriented yaw setpoints obtained from FLORIS retain a positive farm-level benefit when transferred without re-optimization to FAST.Farm. Both models predict the same fundamental redistribution mechanism: the intentionally yawed upstream turbine sacrifices power, while reduced wake overlap increases production downstream. The transferred setpoints produce FAST.Farm gains of approximately 4–5%, and the maximum difference between the imposed-yaw FLORIS and FAST.Farm farm-level predictions is 0.56 percentage points. This agreement supports the use of FLORIS for supervisory setpoint generation in the present multi-fidelity framework, but it does not constitute independent validation of either numerical model.

The imposed-yaw FLORIS comparison and the broader parametric FLORIS analysis serve different purposes. The former evaluates the same yaw vectors transferred to FAST.Farm, whereas the latter independently reoptimizes the yaw offsets at every combination of spacing, wind direction, wind speed, and turbulence intensity. The sensitivity results show that the available aerodynamic benefit is governed primarily by wake-overlap geometry and therefore varies strongly with operating condition. In particular, a small change in wind direction can substantially modify the optimized gain or eliminate it entirely. The 4–5% gain obtained for the coupled reference cases should consequently be interpreted as the response of a controlled, strongly interacting directional sector rather than as a layout-independent wake-steering benefit.

The spacing sensitivity should be interpreted as a comparison among geometrically similar staggered layouts because both Δx and Δy scale with S. The results do not isolate the independent effect of streamwise spacing at a fixed lateral offset. Nevertheless, they demonstrate that the aerodynamic opportunity for wake steering decreases as the overall turbine separation increases and the uncontrolled wakes recover more fully before reaching downstream turbines. Together with the lower 0.921% resource-weighted gain obtained for the Tampen-derived layout, this result confirms that the 4–5% FAST.Farm gain is characteristic of the strongly interacting reference sector and should not be transferred directly to other layouts, turbine ratings, or wind climates.

The resource-weighted Tampen-derived assessment provides a more practical measure of the long-term aerodynamic significance. The annual energy contribution increases by 0.921% over the modeled 4–13 $\mathrm{m\,s^{-1}}$ interval, which is considerably smaller than the gain obtained for the reference four-turbine condition. This reduction reflects the occurrence of wind directions and wind-speed classes for which turbine alignment and wake interaction are weak. The result demonstrates that directional frequency, site wind climate, and layout geometry must be included when translating condition-specific wake-steering gains into long-term energy estimates. The Tampen-derived and parametric FLORIS analyses broaden the aerodynamic-power assessment only and do not extend the coupled FAST.Farm load conclusions to the additional operating conditions.

4.2. Component- and Turbine-Specific Fatigue Response

The fatigue response is not uniformly related to the farm-power benefit. The farm-mean blade-root DEL decreases under all investigated conditions, whereas the tower-base and FairTen1 responses generally increase and the yaw-bearing response changes with wind speed and sea state. More importantly, the turbine-level results show that a favorable or modest farm-mean response can coexist with an adverse localized response. Both farm-mean and turbine-specific metrics are therefore needed to distinguish the aggregate farm response from the fatigue demand experienced by individual turbines. Similar component-dependent power–load trade-offs have been reported in previous wake-steering studies [18,20,21].

The blade-root response reflects competing effects along the turbine row. Intentional yaw misalignment introduces asymmetric rotor loading at the upstream turbines, while reduced wake overlap can alleviate cyclic loading associated with deep- or partial-wake exposure downstream. In the present array, the downstream relief dominates the farm-mean response, but individual turbines can still exhibit positive DEL changes. The negative farm-mean blade-root result should therefore be interpreted as a redistribution of cyclic loading rather than as evidence that wake steering reduces blade fatigue at every turbine.

The tower-base and yaw-bearing responses arise from different dominant mechanisms. The tower-base spectra are separated primarily by sea-state severity over the low-frequency platform pitch/roll and heave range, while the differences between greedy and wake-steering operation are comparatively smaller and distributed over a broad frequency interval. The tower-base DEL increase therefore reflects the interaction of redistributed aerodynamic thrust, hydrodynamic excitation, platform motion, and tower response rather than a purely aerodynamic wake-steering effect [22,23]. By contrast, the yaw-bearing spectra show clearer sensitivity to intentional yaw misalignment in the rotor and structural frequency ranges. Amplification near the 3P and first tower-bending regions is consistent with periodic transmission of asymmetric rotor loading through the hub and nacelle [18,20,21].

The FairTen1 results provide the clearest example of a localized load penalty being concealed by a farm-mean quantity. Although the farm-mean increase remains modest, the turbine-level response reaches approximately 12.8% at T2 under the mild sea state, while T1 experiences a reduction. The largest relative change occurs under mild waves rather than under the condition with the largest absolute fairlead DEL, indicating that wake-steering-induced changes are more prominent relative to a lower environmental baseline. The observed redistribution is consistent with changes in rotor thrust, platform offset, and low-frequency station-keeping response, although the individual aerodynamic and hydrodynamic contributions cannot be separated from the DEL values alone.

The power–load trade-off confirms that farm-power gain is not a reliable proxy for structural acceptability. Conditions producing similar power gains exhibit substantially different tower-base, yaw-bearing, and FairTen1 penalties, while the smallest relative farm-power gain includes the largest localized yaw-bearing response. A power-only optimization objective can therefore transfer fatigue demand to particular turbines or components without revealing that penalty in the farm-power result. Future supervisory optimization should include turbine- and component-specific load constraints, particularly for the yaw bearing, tower base, and station-keeping system, rather than maximizing steady farm power alone.

4.3. Implications for Controller Design and Practical Implementation

Practical implementation would require condition-dependent yaw scheduling based on filtered wind-direction estimates, together with directional persistence, minimum-benefit thresholds, yaw-rate and yaw-travel constraints, and turbine- and component-specific load limits. Floating-platform motion and wake-advection delay further complicate wind-direction estimation and supervisory updating. Consequently, the present power-oriented setpoints should be regarded as candidate supervisory commands rather than a complete operational controller.

4.4. Scope, Uncertainty, and Limitations

The coupled power- and load-response conclusions are restricted to the completed FAST.Farm matrix: three below-rated wind speeds, three sea states, five matched turbulent-inflow realizations, TI $= 6\%$, $WD = 0^\circ$, aligned wind and waves, and the adopted ROSCO controller settings. The simulations assess fixed supervisory yaw offsets under turbulent fluctuations about stationary mean operating conditions. Transitions between wind-speed or wind-direction sectors, repeated setpoint updates, sensing uncertainty, actuator duty, yaw transients, and the associated transient loads were not investigated. The resulting structural, platform, and mooring-load conclusions should therefore not be generalized to other turbulence levels, wind directions, wind–wave-misaligned conditions, or nonstationary supervisory operation.

The complementary FLORIS analyses broaden the steady aerodynamic-power assessment across turbine spacing, wind direction, wind speed, ambient turbulence intensity, and a larger Tampen-derived layout. They do not extend the FAST.Farm load conclusions to those additional conditions because FLORIS does not resolve irregular-wave excitation, floating-platform motion, unsteady wake meandering, structural dynamics, or station-keeping-system response. A single fixed FLORIS model configuration was used throughout these calculations.

The comparison between FLORIS and FAST.Farm should be interpreted as a cross-model consistency assessment within the adopted multi-fidelity workflow rather than independent validation. FAST.Farm is itself an engineering-fidelity numerical model, and comparison with field measurements, controlled experiments, or independently resolved coupled high-fidelity simulations remains necessary to quantify prediction error relative to physical behavior.

Finally, the reported one-hour DELs are comparative fatigue indicators for the investigated operating conditions. They do not establish lifetime cumulative damage, component service-life reduction, structural reliability, or economic benefit. Such conclusions would require long-term damage accumulation over a complete joint metocean and operational distribution, together with component-specific fatigue properties, design constraints, availability, maintenance, repair, and replacement costs.

5. Conclusions

This study assessed whether static power-oriented yaw setpoints obtained with FLORIS retain their farm-level benefit when transferred without re-optimization to a coupled FAST.Farm model of four floating IEA Wind 15 MW turbines. The single-turbine characterization showed that imposed yaw primarily determines wake-center displacement, whereas the investigated curled-wake diffusion parameter primarily affects wake spreading and velocity-deficit recovery. Across three below-rated wind speeds, three sea states, and five matched realizations, static wake steering increased mean farm power in all nine investigated conditions. The paired gains were approximately 5.1–5.2% at 7 $\mathrm{m\,s^{-1}}$, 5.0–5.1% at 8 $\mathrm{m\,s^{-1}}$, and 4.0–4.2% at 9 $\mathrm{m\,s^{-1}}$, with all paired 95% confidence intervals above zero. The local loss at T1 was exceeded by the combined recovery of T2–T4, producing net increases of 0.633, 0.920, and 1.062 MW, respectively.

The fatigue response was component- and turbine-specific. The farm-mean blade-root DEL decreased under all investigated conditions, the tower-base DEL increased, the yaw-bearing response changed sign with operating condition, and FairTen1 generally increased. Turbine-level penalties reached approximately 10.4% for the yaw-bearing DEL and 12.8% for FairTen1, demonstrating that farm-mean quantities can conceal localized adverse responses. The spectral results associate the yaw-bearing changes with yaw-induced rotor and structural excitation, including the 3P and first tower-bending ranges, whereas the tower-base response is dominated by low-frequency sea-state and floating-platform dynamics with smaller control-related differences superimposed.

The complementary FLORIS analyses showed that the optimized steady aerodynamic benefit is governed primarily by wind direction and turbine spacing, with additional modulation by wind speed and ambient turbulence intensity. The 4–5% gain obtained for the strongly interacting four-turbine reference sector should therefore not be transferred directly to arbitrary layouts or long-term operation. For the Tampen-derived 11-turbine layout, resource weighting over the modeled 4–13 m s^{-1} interval increased the annual energy contribution from 396.489 to 400.142 GWh $year^{-1}$, corresponding to 3.653 GWh $year^{-1}$, or 0.921%.

These results provide numerical evidence, within the adopted models and operating matrix, that static wake steering can retain a positive farm-power benefit in a coupled floating wind-farm environment. Controller assessment should therefore combine farm power with turbine- and component-specific structural and mooring-load constraints. The coupled load conclusions remain restricted to TI = 6%, $WD = 0^\circ$, aligned wind and waves, stationary mean operating conditions, and the adopted controller settings, while the FLORIS extensions address aerodynamic power only. The reported one-hour DELs do not establish lifetime damage or economic benefit, and the FLORIS–FAST.Farm comparison is a consistency assessment rather than independent validation.

Author Contributions: Conceptualization, M.E., A.F., S.M. and M.B.; methodology, M.E., F.B. and A.F.; software, M.E. and F.B.; validation, M.E., F.B. and A.F.; formal analysis, M.E.; investigation, M.E.; resources, A.F., S.M. and M.B.; data curation, M.E.; writing—original draft preparation, M.E.; writing—review and editing, M.E., F.B., A.F., S.M. and M.B.; visualization, M.E.; supervision, A.F., S.M. and M.B.; project administration, S.M. and M.B.; funding acquisition, S.M. and M.B. All authors have read and agreed to the published version of the manuscript.

Funding: This research received no external funding.

Data Availability Statement: The data supporting the findings of this study are available from the corresponding author upon reasonable request.

Acknowledgments: The authors acknowledge the financial support for their doctoral scholarships within the framework of the Italian National Recovery and Resilience Plan (PNRR), with co-funding from Eni S.p.A. The authors acknowledge CFDHub@Polimi, the interdepartmental high-performance computing infrastructure of Politecnico di Milano, for providing the computational resources used in this study.

Conflicts of Interest: The authors declare no conflicts of interest.

Abbreviations

The following abbreviations are used in this manuscript:

1P, 2P, 3P	One-, two-, and three-per-revolution rotor harmonics
BEM	Blade-element momentum
DEL	Damage-equivalent load
DWM	Dynamic wake meandering
FAST.Farm	FAST wind-farm simulation tool
FLORIS	FLOw Redirection and Induction in Steady State
GCH	Gauss–curl hybrid
IEA	International Energy Agency
IEC	International Electrotechnical Commission
JONSWAP	Joint North Sea Wave Project
LES	Large-eddy simulation
MLife	Fatigue post-processing tool
PSD	Power spectral density
ROSCO	Reference Open-Source Controller
SAMWICH	Simulated And Measured Wake Identification and CHaracterization
TI	Turbulence intensity
URANS	Unsteady Reynolds-averaged Navier–Stokes
WAT	Wake-added turbulence
ZeroMQ	Zero Message Queue

Appendix A. Additional FAST.Farm Results

Table A1. Complete statistics for the farm-mean damage-equivalent-load changes. For each load component, wind speed, and sea state, the table reports the mean paired relative change in the farm-mean DEL, the sample standard deviation across the five matched turbulent-inflow realizations, and the corresponding 95% confidence interval. The final column identifies the turbine with the maximum numerical turbine-level mean paired DEL change and gives the corresponding value. All statistics are based on $n = 5$ matched turbulent-inflow realizations.

Component	U [m s^{-1}]	Sea State	Farm-Mean ΔDEL [%]	Seed SD [pp]	95% CI [%]	Maximum Mean Turbine-Level ΔDEL
Blade-root	7	Mild	−0.85	0.02	[−0.88, −0.82]	T4: −0.24%
		Medium	−0.84	0.03	[−0.87, −0.81]	T4: −0.26%
		Severe	−0.82	0.05	[−0.88, −0.75]	T4: −0.21%
	8	Mild	−1.29	0.07	[−1.37, −1.20]	T4: +0.01%
		Medium	−1.28	0.08	[−1.38, −1.18]	T4: −0.02%
		Severe	−1.25	0.10	[−1.37, −1.12]	T4: +0.01%
	9	Mild	−2.03	0.14	[−2.21, −1.85]	T2: +0.70%
		Medium	−2.03	0.16	[−2.23, −1.83]	T2: +0.99%
		Severe	−2.24	0.37	[−2.70, −1.77]	T2: +1.46%
Tower-base	7	Mild	+1.59	0.33	[+1.18, +1.99]	T2: +4.02%
		Medium	+0.82	0.14	[+0.65, +0.99]	T2: +1.66%
		Severe	+0.76	0.07	[+0.67, +0.85]	T2: +1.49%
	8	Mild	+2.26	0.76	[+1.31, +3.21]	T2: +5.29%
		Medium	+0.96	0.07	[+0.87, +1.05]	T2: +1.86%
		Severe	+0.88	0.15	[+0.69, +1.06]	T2: +1.93%
	9	Mild	+2.78	0.71	[+1.89, +3.67]	T2: +6.71%
		Medium	+1.35	0.10	[+1.23, +1.48]	T2: +3.13%
		Severe	+1.12	0.11	[+0.98, +1.26]	T2: +2.55%
Yaw-bearing	7	Mild	+3.37	0.76	[+2.43, +4.31]	T2: +5.72%
		Medium	−0.84	0.43	[−1.37, −0.31]	T4: +0.86%
		Severe	−1.15	0.22	[−1.42, −0.88]	T4: +0.59%
	8	Mild	+3.28	0.30	[+2.91, +3.66]	T2: +6.41%
		Medium	−0.29	0.42	[−0.81, +0.24]	T4: +1.71%
		Severe	−0.93	0.60	[−1.67, −0.18]	T4: +1.10%
	9	Mild	+4.32	0.53	[+3.67, +4.98]	T2: +10.42%
		Medium	+0.41	0.62	[−0.36, +1.17]	T2: +3.83%
		Severe	−0.19	0.33	[−0.61, +0.22]	T2: +2.28%
FairTen1	7	Mild	+2.92	2.18	[+0.21, +5.63]	T2: +12.79%
		Medium	+1.32	0.30	[+0.95, +1.69]	T2: +4.52%
		Severe	+0.88	0.19	[+0.64, +1.12]	T2: +2.50%
	8	Mild	+2.02	1.65	[−0.04, +4.07]	T2: +8.53%
		Medium	+1.15	0.45	[+0.59, +1.72]	T2: +4.63%
		Severe	+1.90	0.28	[+1.56, +2.25]	T2: +4.56%
	9	Mild	+2.05	0.74	[+1.14, +2.97]	T2: +5.39%
		Medium	+1.49	0.33	[+1.07, +1.90]	T2: +5.35%
		Severe	+1.26	0.10	[+1.14, +1.38]	T2: +3.57%

Notes: For each matched turbulent-inflow realization, the absolute DEL was first averaged across the four turbines separately for greedy and static wake-steering operation. The paired relative change in this farm-mean DEL was then calculated, and the reported mean and sample standard deviation were obtained from the five resulting seed-level values. SD is reported in percentage points (pp), and the 95% confidence interval was calculated using the Student-t distribution with four degrees of freedom. The final column identifies the turbine with the maximum numerical turbine-level mean paired DEL change after each turbine's paired response was averaged across the five realizations. This differs from the seed-wise worst-turbine metric used in the power–load trade-off figure, where the maximum is selected independently within each realization before statistical aggregation. Positive values indicate increased fatigue loading under static wake steering, whereas negative values indicate reduced fatigue loading.

References

1. Barthelmie, R.J.; Pryor, S.C.; Frandsen, S.T.; Hansen, K.S.; Schepers, J.; Rados, K.; Schlez, W.; Neubert, A.; Jensen, L.; Neckelmann, S. Quantifying the impact of wind turbine wakes on power output at offshore wind farms. *J. Atmos. Ocean. Technol.* **2010**, *27*, 1302–1317. [CrossRef]
2. Porté-Agel, F.; Bastankhah, M.; Shamsoddin, S. Wind-turbine and wind-farm flows: A review. *Bound. Layer Meteorol.* **2020**, *174*, 1–59. [CrossRef] [PubMed]
3. Thomsen, K.; Sørensen, P. Fatigue loads for wind turbines operating in wakes. *J. Wind Eng. Ind. Aerodyn.* **1999**, *80*, 121–136. [CrossRef]
4. Knudsen, T.; Bak, T.; Svenstrup, M. Survey of wind farm control—Power and fatigue optimization. *Wind Energy* **2015**, *18*, 1333–1351. [CrossRef]
5. Boersma, S.; Doekemeijer, B.; Vali, M.; Meyers, J.; van Wingerden, J.W. A control-oriented dynamic wind farm model: WFSim. *Wind Energy Sci.* **2018**, *3*, 75–95. [CrossRef]
6. Meyers, J.; Bottasso, C.; Dykes, K.; Fleming, P.; Gebraad, P.; Giebel, G.; Göçmen, T.; Van Wingerden, J.W. Wind farm flow control: Prospects and challenges. *Wind Energy Sci.* **2022**, *7*, 2271–2306. [CrossRef]
7. Goit, J.P.; Meyers, J. Optimal control of energy extraction in wind-farm boundary layers. *J. Fluid Mech.* **2015**, *768*, 5–50. [CrossRef]
8. Munters, W.; Meyers, J. Effect of wind turbine response time on optimal dynamic induction control of wind farms. *J. Phys. Conf. Ser.* **2016**, *753*, 052007. [CrossRef]
9. van der Hoek, D.; Kanev, S.; Allin, J.; Bieniek, D.; Mittelmeier, N. Effects of axial induction control on wind farm energy production—A field test. *Renew. Energy* **2019**, *140*, 994–1003. [CrossRef]
10. Bossanyi, E.; Ruisi, R. Axial induction controller field test at Sedini wind farm. *Wind Energy Sci.* **2021**, *6*, 389–408. [CrossRef]
11. Bastankhah, M.; Porté-Agel, F. Experimental and theoretical study of wind turbine wakes in yawed conditions. *J. Fluid Mech.* **2016**, *806*, 506–541. [CrossRef]
12. Fleming, P.; Annoni, J.; Churchfield, M.; Martinez-Tossas, L.A.; Gruchalla, K.; Lawson, M.; Moriarty, P. A simulation study demonstrating the importance of large-scale trailing vortices in wake steering. *Wind Energy Sci.* **2018**, *3*, 243–255. [CrossRef]
13. Howland, M.F.; Bossuyt, J.; Martínez-Tossas, L.A.; Meyers, J.; Meneveau, C. Wake structure in actuator disk models of wind turbines in yaw under uniform inflow conditions. *J. Renew. Sustain. Energy* **2016**, *8*, 043301. [CrossRef]
14. Bartl, J.; Mühle, F.; Schottler, J.; Sætran, L.; Peinke, J.; Adaramola, M.; Hölling, M. Wind tunnel experiments on wind turbine wakes in yaw: Effects of inflow turbulence and shear. *Wind Energy Sci.* **2018**, *3*, 329–343. [CrossRef]
15. Mao, X.; Sørensen, J. Far-wake meandering induced by atmospheric eddies in flow past a wind turbine. *J. Fluid Mech.* **2018**, *846*, 190–209. [CrossRef]
16. Vollmer, L.; Steinfeld, G.; Heinemann, D.; Kühn, M. Estimating the Wake Deflection Downstream of a Wind Turbine in Different Atmospheric Stabilities: An LES Study. *Wind Energy Sci.* **2016**, *1*, 129–141. [CrossRef]
17. Branlard, E.; Martínez-Tossas, L.A.; Jonkman, J. A time-varying formulation of the curled wake model within the FAST. Farm framework. *Wind Energy* **2023**, *26*, 44–63. [CrossRef]
18. Damiani, R.; Dana, S.; Annoni, J.; Fleming, P.; Roadman, J.; van Dam, J.; Dykes, K. Assessment of wind turbine component loads under yaw-offset conditions. *Wind Energy Sci.* **2018**, *3*, 173–189. [CrossRef]
19. White, J.; Ennis, B.; Herges, T.G. Estimation of rotor loads due to wake steering. In Proceedings of the 2018 Wind Energy Symposium, Kissimmee, FL, USA, 8–12 January 2018. [CrossRef]
20. Thedin, R.; Kreeft, J.; Barter, G.; Jonkman, J.; Shaler, K. Impact of wake steering on loads of downstream wind turbines at an above-rated condition. In *Proceedings of the Journal of Physics: Conference Series*; IOP Publishing: Bristol, UK, 2024; Volume 2767, p. 032020.
21. Thedin, R.; Barter, G.; Jonkman, J.; Mudafort, R.; Bay, C.J.; Shaler, K.; Kreeft, J. Load assessment of a wind farm considering negative and positive yaw misalignment for wake steering. *Wind Energy Sci.* **2025**, *10*, 1033–1053. [CrossRef]
22. Ramos-García, N.; González Horcas, S.; Pegalajar-Jurado, A.; Kontos, S.; Bredmose, H. Investigation of the floating IEA wind 15-MW RWT using vortex methods Part II: Wake impact on downstream turbines under turbulent inflow. *Wind Energy* **2022**, *25*, 1434–1463. [CrossRef]
23. Carmo, L.; Jonkman, J.; Thedin, R. Investigating the interactions between wakes and floating wind turbines using FAST. Farm. *Wind Energy Sci.* **2024**, *9*, 1827–1847. [CrossRef]
24. Liu, S.; Xin, Z.; Wang, L.; Xu, Y.; Cai, Z. Fluid–structure interaction simulation of the effect of static yaw control on the aerodynamic responses and wake characteristics of floating offshore wind turbines. *Energy* **2025**, *330*, 136589. [CrossRef]
25. Liang, Z.; Liu, H. Novel yaw-based wake modelling and controlling to enhance the power output of floating offshore wind farms. *Renew. Energy* **2026**, *256*, 123838. [CrossRef]

26. Martinez-Tossas, L.A.; Churchfield, M.J.; Yilmaz, A.E.; Sarlak, H.; Johnson, P.L.; Sørensen, J.N.; Meyers, J.; Meneveau, C. Comparison of four large-eddy simulation research codes and effects of model coefficient and inflow turbulence in actuator-line-based wind turbine modeling. *J. Renew. Sustain. Energy* **2018**, *10*, 033301. [CrossRef]
27. Fleming, P.; King, J.; Bay, C.J.; Simley, E.; Mudafort, R.; Hamilton, N.; Farrell, A.; Martínez-Tossas, L.A. Overview of FLORIS Updates. *J. Phys. Conf. Ser.* **2020**, *1618*, 022028. [CrossRef]
28. Jonkman, J.M.; Annoni, J.; Hayman, G.; Jonkman, B.; Purkayastha, A. Development of FAST.Farm: A New Multi-Physics Engineering Tool for Wind-Farm Design and Analysis. In Proceedings of the 35th Wind Energy Symposium, Grapevine, TX, USA, 9–13 January 2017. [CrossRef]
29. Rivera-Arreba, I.; Li, Z.; Yang, X.; Bachynski-Polić, E.E. Comparison of the dynamic wake meandering model against large eddy simulation for horizontal and vertical steering of wind turbine wakes. *Renew. Energy* **2024**, *221*, 119807. [CrossRef]
30. Zhang, T.; Xu, X.; Wang, S.; Xing, Y.; Dou, P.; Ji, R.; Yang, P. Investigation of wake steering control effects on the dynamic responses of 15 MW semi-submersible floating wind farms. *Renew. Energy* **2025**, *254*, 123704. [CrossRef]
31. Mohammadi, M.; Bossanyi, E.; Harrison, M.; Ogbeifun, M.; McCarthy, C.; Chapman, J.; Bastankhah, M.; Landberg, L. Feasibility Study of implementing Wake Steering in Floating Wind Farms: Power Gain, Load Estimation and Economic Analysis. *Wind Energy* **2026**, *29*, e70111. [CrossRef]
32. Allen, C.; Viselli, A.; Dagher, H.; Goupee, A.; Gaertner, E.; Abbas, N.; Hall, M.; Barter, G. *Definition of the UMaine VolturnUS-S Reference Platform Developed for the IEA Wind 15-Megawatt Offshore Reference Wind Turbine*; Technical Report NREL/TP-5000-76773; National Renewable Energy Laboratory: Golden, CO, USA, 2020.
33. Tenggren, E.; Erik Olsen, L.; Andre Johansen, D.; Bracchi, T. A numerical study on the effect of wind turbine wake meandering on the power production of hywind tampen. In *Proceedings of the Journal of Physics: Conference Series*; IOP Publishing: Bristol, UK, 2020; Volume 1669, p. 012026.
34. Haakenstad, H.; Breivik, Ø.; Furevik, B.R.; Reistad, M.; Bohlinger, P.; Aarnes, O.J. NORA3: A nonhydrostatic high-resolution hindcast of the North Sea, the Norwegian Sea, and the Barents Sea. *J. Appl. Meteorol. Climatol.* **2021**, *60*, 1443–1464. [CrossRef]
35. Solbrekke, I.M.; Sorteberg, A.; Haakenstad, H. The 3 km Norwegian reanalysis (NORA3)—A validation of offshore wind resources in the North Sea and the Norwegian Sea. *Wind Energy Sci.* **2021**, *6*, 1501–1519. [CrossRef]
36. Gaertner, E.; Rinker, J.; Sethuraman, L.; Zahle, F.; Anderson, B.; Barter, G.; Abbas, N.; Meng, F.; Bortolotti, P.; Skrzypinski, W.; et al. *Definition of the IEA 15-Megawatt Offshore Reference Wind Turbine*; Technical Report NREL/TP-5000-75698; National Renewable Energy Laboratory: Golden, CO, USA, 2020.
37. Jonkman, B.; Mudafort, R.M.; Platt, A.; Branlard, E.; Sprague, M.; Ross, H.; Hall, M.; Slaughter, D.; Vijayakumar, G.; Buhl, M.; et al. OpenFAST/openfast: v3.5.0. Zenodo 2024. Available online: https://zenodo.org/records/7942867 (accessed on 8 August 2026).
38. Abbas, N.J.; Zalkind, D.S.; Pao, L.; Wright, A. A reference open-source controller for fixed and floating offshore wind turbines. *Wind Energy Sci.* **2022**, *7*, 53–73. [CrossRef]
39. Gupta, A. Add Various Features and Tests to ZeroMQ wind Farm Control Implementation. GitHub Pull Request #282, NatLabRockies/ROSCO, 2023. Merged 5 December 2023. Available online: https://github.com/NatLabRockies/ROSCO/pull/282 (accessed on 8 August 2026).
40. Krathe, V.L.; Thedin, R.; Jonkman, J.M.; Nejad, A.R.; Bachynski-Polić, E.E. Main bearing response in a waked 15-MW floating wind turbine in below-rated conditions. *Forsch. Ingenieurwesen* **2025**, *89*, 37. [CrossRef]
41. Bellini, F.; Ebrahimi, M.; Giuseppe, P.D.; Fontanella, A.; Muggiasca, S.; Belloli, M. Closed-loop Wind farm control for floating turbines via online yaw and induction setpoint optimization. *Proc. J. Phys. Conf. Ser.* **2026**, *3224*, 032081. [CrossRef]
42. King, J.; Fleming, P.; King, R.; Martínez-Tossas, L.A.; Bay, C.J.; Mudafort, R.; Simley, E. Controls-oriented model for secondary effects of wake steering. *Wind Energy Sci.* **2021**, *6*, 701–714. [CrossRef]
43. Fleming, P.A.; Stanley, A.P.; Bay, C.J.; King, J.; Simley, E.; Doekemeijer, B.M.; Mudafort, R. Serial-refine method for fast wake-steering yaw optimization. In *Proceedings of the Journal of Physics: Conference Series*; IOP Publishing: Bristol, UK, 2022; Volume 2265, p. 032109.
44. Türk, M.; Emeis, S. The dependence of offshore turbulence intensity on wind speed. *J. Wind. Eng. Ind. Aerodyn.* **2010**, *98*, 466–471. [CrossRef]
45. Jeans, G. Converging profile relationships for offshore wind speed and turbulence intensity. *Wind Energy Sci.* **2023**, *9*, 2001–2015. [CrossRef]
46. Liew, J.; Urbán, A.M.; Andersen, S.J. Analytical model for the power–yaw sensitivity of wind turbines operating in full wake. *Wind Energy Sci.* **2020**, *5*, 427–437. [CrossRef]
47. Quon, E.W. SAMWICH Box: A Python-Based Toolbox for Simulated and Measured Wake Identification and Characterization. 2017. Available online: https://github.com/ewquon/waketracking (accessed on 16 June 2026).

48. Quon, E.W.; Doubrawa, P.; Debnath, M. Comparison of rotor wake identification and characterization methods for the analysis of wake dynamics and evolution. In *Proceedings of the Journal of Physics: Conference Series*; IOP Publishing: Bristol, UK, 2020; Volume 1452, p. 012070.
49. Jonkman, B.J. *TurbSim User's Guide v2.00.00*; National Renewable Energy Laboratory: Golden, CO, USA, 2014.